Modified Co/TiO2 catalysts for CO2 hydrogenation to fuels

Canio Scarfiello, Katerina Soulantica, Simon Cayez, Aurélien Durupt, Guillaume Viau, Nolwenn Le Breton, Athanassios Boudalis, Frédéric Meunier, Guillaume Clet, Mathias Barreau, et al.

Modified Co/TiO_2 catalysts for CO_2 hydrogenation to fuels

Canio Scarfiello,[a,b,c] Katerina Soulantica,[b] Simon Cayez,[b] Aurélien Durupt,[a,b,c] Guillaume Viau,[b] Nolwenn Le Breton,[d] Athanassios K. Boudalis,[d] Frédéric Meunier,[e] Guillaume Clet,[f] Mathias Barreau,[g] Davide Salusso,[h] Spiros Zafeiratos,[g] Doan Pham Minh,[a] Philippe Serp[c]

[a] *Université de Toulouse, IMT Mines Albi, UMR CNRS 5302, Centre RAPSODEE, Campus Jarlard, F-81013 Albi, cedex 09, France.*

[b] *Université de Toulouse, INSA, UPS, CNRS, LPCNO, 135 avenue de Rangueil, F-31077 Toulouse, France.*

[c] *LCC, CNRS-UPR 8241, ENSIACET, Université de Toulouse, France.*

[d] *Institut de Chimie de Strasbourg, Université de Strasbourg-CNRS UMR 7177, 4 rue Blaise Pascal, BP 296 R8, F-67008 Strasbourg Cedex, France*

[e] *Université Claude Bernard Lyon 1, CNRS, IRCELYON, 2 Av. Albert Einstein, F-69626 Villeurbanne, France.*

[f] *Normandie Univ, ENSICAEN, UNICAEN, CNRS, LCS, F-14000 Caen, France*

[g] *ICPEES-UMR 7515 CNRS-ECPM-Université de Strasbourg, 25, rue Becquerel, F-67087 Strasbourg Cedex 2, FRANCE*

[h] *European Synchrotron Radiation Facility, CS 40220, Cedex 9 F-38043 Grenoble, France*

Keywords: CO_2 hydrogenation, promotion effects, alkali metals, hydrogen spillover, synergistic effect

Abstract. The direct CO_2 conversion to liquid fuels by catalytic hydrogenation (CO_2-based Fischer-Tropsch synthesis, FTS), is a sustainable approach to reduce CO_2 emissions. This challenging reaction proceeds through tandem catalysis involving reverse water gas shift reaction to produce CO and subsequent traditional CO-FTS. Unmodified Co-based catalysts allow performing the reaction at low temperatures (< 250 °C), albeit producing mainly methane. In this study, we modified a commercial TiO_2-P25 support by $NaBH_4$ reduction so as to introduce controlled amounts of promoters and oxygen vacancies (O_v). The modified and unmodified supports were used to prepare Co-based catalysts, which were evaluated for CO_2-based FTS at 220-250 °C and 20 bar. The promoted catalysts outperform the one prepared on commercial TiO_2 in terms of activity and selectivity towards C_{5+}. Detailed characterizations of the catalysts were performed to decipher the role of promoters. We show that, besides

improving CO_2 activation and limiting H_2 activation, the presence of alkali on the support allows a modulation of hydrogen spillover in the system. The best catalyst in terms of activity and selectivity is the one for which sodium is deposited in sufficient amount to modulate the hydrogen spillover, which allows an optimal surface C/H ratio on cobalt.

1. Introduction

Carbon dioxide catalytic hydrogenation with H_2 produced from nuclear or renewable energies is a promising way toward carbon neutralization, while producing value-added fuels such as methane, long-chain hydrocarbons, olefins, methanol, or higher alcohols [1]. The selective production of C_{2+} hydrocarbons by one-step CO_2 hydrogenation (CO_2-based Fischer-Tropsch synthesis, CO_2-FTS) is particularly challenging due to the high C−C coupling barriers, and the numerous competing reactions generating undesired C_1 products. During the one-step CO_2-FTS, the exothermic FT reaction (Eq. 1) occurs only after the initial transformation of CO_2 into CO *via* the reverse water gas-shift reaction (RWGS, Eq. 2). As the latter is slightly endothermic, CO_2 conversion to CO is often limited at the temperatures required for FTS.

$$n\mathrm{CO} + (2n+1)\mathrm{H_2} \rightarrow \mathrm{C}_n\mathrm{H}_{2n+2} + n\mathrm{H_2O} \qquad \Delta H_{298} = -165\ \mathrm{kJ{\cdot}mol^{-1}} \qquad \text{(Eq.1)}$$

$$\mathrm{CO_2} + \mathrm{H_2} \rightarrow \mathrm{CO} + \mathrm{H_2O} \qquad \Delta H_{298} = 41.2\ \mathrm{kJ{\cdot}mol^{-1}} \qquad \text{(Eq.2)}$$

Iron-based catalysts are relatively active for RWGS, but need harsher conditions than Co-based catalysts and show high deactivation rates during the traditional FTS [2, 3]. Indeed, metallic cobalt represents one of the best choices for the production of synthetic hydrocarbons *via* traditional FTS [4]. However, for CO_2-FTS on cobalt catalysts, weak CO_2 adsorption and RWGS thermodynamic constraints lead to low C/H surface ratio and CO coverage, resulting in the preferential production of CH_4 and short chain hydrocarbons [5].
Several parameters can be modulated to improve the selectivity towards C_{2+} products on Co-based catalysts such as: the choice of cobalt active phase, support and metal support interfaces, and the addition of promoters [6]. The role of the different Co active phases is still debated in the literature [7]. Both metallic cobalt and cobalt oxide (CoO) can be active during CO_2-FTS, depending on the support used [8]. Metallic cobalt is more active on most supports, while CoO appears to be an alternative choice on titania [8, 9]. The formation of a unique interface between cobalt and the TiO_2 support could be at the origin of this behavior. Cobalt carbides seem to be related to the formation of methane or ethanol, depending on the support [10], as well as to catalyst deactivation [7]. However, a recent work reports that specific facets of Co_2C display excellent RWGS and CO_2-FTS activity for the direct synthesis of olefins and alcohols [11]. As far as the support is concerned, reducible oxides and especially TiO_2 are better adapted for this reaction than irreducible oxides [6]. The higher activity obtained on TiO_2-based catalysts stems from the ability of reducible oxides to create unique metal-support interfaces, originating from strong metal-support interaction (SMSI) [12], which can largely benefit the CO_2 activation toward different products, from C_{2+} to CH_4 and CO [7, 9]. Moreover, reducible oxides and metal-oxide interfaces are rich in surface defects such as reduced cationic sites or oxygen vacancies (O_v) that can be exploited for the direct activation of CO_2 [13, 14]. Such surface defects, when properly introduced on a reducible support, can also enhance metal dispersion during catalyst preparation [15]. It was also demonstrated that the crystal phase of TiO_2 (rutile or anatase) has a significant effect on the product selectivity obtained on Co-based catalysts [16]. Finally, the addition of alkali promoters allows increasing CO_2 adsorption, C/H surface ratio and the intrinsically marginal activity of Co-based catalysts for RWGS, helping to mitigate excess methanation and to increase overall C_{2+} selectivity [6, 16, 17]. Moreover, alkali and

alkaline earth promotion can also favor the generation of O_v on reducible supports, and improve the final metal dispersion [18].
The present study aims at disentangling the effects of the support modification on the CO_2-FTS using Co/TiO_2 catalysts. Compared to the work of Li and coworkers [16], in which TiO_2 anatase and rutile phase were compared, we used in our study a TiO_2 support containing a mixture of anatase and rutile phase (TiO_2-P25), since such mixtures have been shown to be advantageous for the CO-FTS [19]. Commercial TiO_2-P25 was partially reduced using $NaBH_4$ as reducing agent, leading to the formation of surface defects (O_v and Ti^{3+}) and the incorporation of Na and B promoters. The amount of both surface defects and promoters can be controlled by modulating the conditions of the reduction process. The resulting modified supports were employed for the preparation of Co-based catalysts by incipient wetness impregnation (IWI), and the resulting catalysts were evaluated for the direct CO_2-FTS at 220 and 250 °C. The catalysts prepared on different modified supports outperform the one prepared on the commercial TiO_2-P25 (benchmark), in terms of selectivity towards C_{2+} and C_{5+}. The catalysts showing low alkali loading are also more active than the one prepared on the commercial support. We show through *ex situ* and *in situ* analyses that the presence of sodium in the catalyst affects catalytic performance in several ways. First of all, the promoter contributes to the activation of CO_2, which contributes to the catalytic activity. The localization of the promoter, on the support and/or on the metal also has a marked effect on the activity and the selectivity. When the promoter interacts with cobalt, the activity decreases but the selectivity increases relative to the unmodified catalyst. When sodium is essentially present on the support, it also serves to modulate the hydrogen spillover in the system. This regulation of hydrogen spillover makes it possible to achieve high activities and selectivity in C_{5+}.

2. Results and discussion

2.1 Titania support modification. The reduction of TiO_2 with $NaBH_4$ (Eq. 3) has already been used for the preparation of colored crystalline core/amorphous shell structures ($TiO_2@TiO_{2-x}$) with superior photocatalytic properties [20, 21], including for photocatalytic CO_2 conversion [22]. This reduction process produces different defect states within the bandgap of TiO_2, which are accompanied by a drastic color change. After reduction of commercial TiO_2-P25 containing 85% anatase (A-TiO_2) and 15% rutile (R-TiO_2), the white color of the material changes into blue or black, depending on the temperature treatment [23].

$$8Ti^{4+} + NaBH_4 + 2H_2O \rightarrow 8Ti^{3+} + NaBO_2 + 8H^+ \qquad \text{(Eq. 3)}$$

Here, this reduction process was implemented to obtain different supports for the preparation of Co-based catalysts for CO_2-FTS. Careful control of the operating conditions such as amount of $NaBH_4$, reaction temperature and washing steps, allows: i) the modulation of the final TiO_2 reduction degree (concentration of O_v and Ti^{3+}) and, ii) the incorporation of various amounts of Na and B promoters in the modified titania support (denoted as TiO_2*).
Mild reduction leads to the formation of the m-TiO_2* support, characterized by a medium concentration of defects (O_v, Ti^{3+}) and promoters (Na, B), and showing a light-blue color (**Figure S1**). Harsher reduction conditions lead to the formation of the dark-blue d-TiO_2* support, rich in surface defects and promoters (**Table 1**). Finally, the reoxidation of the m-TiO_2* support under air leads to the formation of the white m-TiO_2*-reox support (**Figure S1**), deprived of surface defects and containing only the promoters. Only small differences of promoter concentrations are detected between the m-TiO_2* and m-TiO_2*-reox supports, in line

with small variations obtained among different batches (Na wt% can vary between 0.5 and 0.7 wt% on m-TiO_2* and between 1.1 and 1.3 wt% for d-TiO_2*).

Table 1. Promoter and defect concentration on the different supports according to ICP-OES and EPR analyses, respectively.

Support	ICP-OES (%wt)		Total spin concentration[a] (nmol.mg^{-1})	Approximate relative concentrations[a]	
	Na	B		O_v (%)	Ti^{3+} (%)
TiO_2	-	-	< 1	0	100
m-TiO_2*	0.52	0.02	480	< 0.1	99.9
d-TiO_2*	1.18	0.07	1000	< 0.1	99.9
m-TiO_2*-reox	0.50	0.02	< 10	< 0.1	99.9

[a] Based on double integration of the EPR signal.

Electron paramagnetic resonance (EPR) spectroscopy was used to confirm the presence of unpaired electrons, O_v and Ti^{3+} in the different supports. The EPR spectra of the supports are shown in the **Figure 1a**, and the main results are summarized in **Table 1**. On the commercial TiO_2-P25, only an extremely weak signal centered at g = 1.97 can be detected, assigned to a small amount of Ti^{3+} [24], resulting in a very low total radical concentration (< 1 nmol/mg). Upon reduction, the total concentration of radical species increases significantly up to 480 nmol.mg^{-1} and 1 μmol.mg^{-1} for m-TiO_2* and d-TiO_2*, respectively. Moreover, a second peak centered at g = 2.002, which can be assigned to O_v, starts to be visible (**Figure 1a**) [24]. Both signals are still visible on the m-TiO_2*-reox, even if the total radical concentration decreased significantly (< 10 nmol.mg^{-1}). Such signals can be attributed to residual defects in the subsurface layers of the support, likely related to the presence of promoter incorporation [25]. Overall, the EPR results confirm the creation of defects (O_v and Ti^{3+}) upon reduction with $NaBH_4$, and the destruction of almost all these defects upon reoxidation in air.

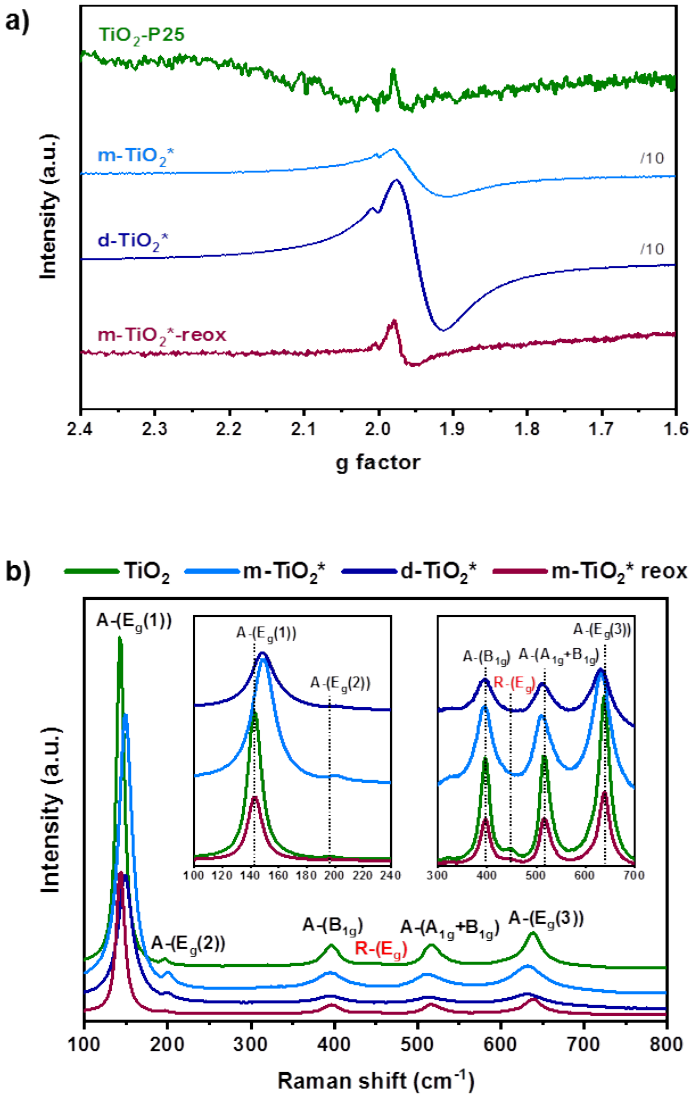

Figure 1. a) EPR spectra recorded at 100 K of the different supports normalized to the sample mass. The intensities of the spectra of the two reduced supports (m-TiO_2* and d-TiO_2*) were divided by 10. **b)** Raman spectra of the different supports. A = TiO_2-anatase; R = TiO_2-rutile.

Raman analyses were performed (**Figure 1b**) to confirm the presence of disorder and O_v. For TiO_2-P25, the main Raman bands appear at ~ 143, 196, 397, 516, and 638 cm^{-1}, which are all ascribable to the predominant A-TiO_2 phase [26]. Only one weak band of R-TiO_2 at ~ 447 cm^{-1} (R-(E_g)) appears on TiO_2 (**Figure 1b**, inset). The latter is no more visible upon reduction (m-TiO_2* and d-TiO_2*), which is consistent with an easier reducibility of the R-TiO_2 phase [27]. Finally, this band appears again upon reoxidation on the m-TiO_2*-reox support, in line with XRD results (*vide infra*). Anatase bands also show some shift upon the different treatments. In particular, the lowest frequency vibrational mode of A-TiO_2 $E_g(1)$ at 143 cm^{-1} shows significant broadening, and shifts towards higher wavenumbers (blue-shift) in m-TiO_2* and d-TiO_2*. Such broadening and blue shift of the $E_g(1)$ mode in Na-doped TiO_2 has been attributed to a decrease of the particle size and non-stoichiometry related to defect formation [28]. The small changes in the A-TiO_2 crystallite size (*vide infra*) and the disappearance of this blue shift upon reoxidation (**Figure 1b**, inset) suggest that non-stoichiometry (O_v and Ti^{3+}) should be

responsible for the variation of the $E_g(1)$ mode. Conversely, a small red shift can be detected, on both m-TiO_2* and d-TiO_2*, for the A-TiO_2 bands at higher wavenumbers (397, 516, and 638 cm^{-1}). This red shift can be tentatively attributed to the incorporation of Na into these two samples [29].

Commercial TiO_2 is a mixture of A-TiO_2 and R-TiO_2. Furthermore, a small amount of amorphous phase was detected by TEM [30]. The XRD diffractograms of the supports are shown in **Figure S2**. The rutile content was estimated from the XRD peak intensity using Eq. 4 [31, 32].

$$\chi = (1 + 0.8\, I_{A(101)}/I_{R(110)})^{-1} \quad \text{(Eq. 4)}$$

The estimated crystallite size, the 2θ values of A-TiO_2(101) and R-TiO_2(110) planes, and the estimated rutile content in the different samples are listed in the **Table S1**. Upon reduction of TiO_2, a diffraction peak at ~ 49.6° starts to be visible on the m-TiO_2* support, which can be attributed to the sodium titanate $Na_{0.46}TiO_2$ phase [33]. Small shifts towards lower 2θ values can be detected for both A-TiO_2(101) and R-TiO_2(110) diffraction peaks upon support reduction (**Table S1**), which can be attributed to the formation of surface defects [34], and of the new sodium titanate phase. This phase becomes significantly more visible on the d-TiO_2* support, in line with the higher sodium content in this sample. Moreover, new peaks ascribable to $Na_2B_6O_{10}$, Na_2O, $NaBO_2$, and B_2O can be detected on this latter support, in line with the results of other authors [20]. None of these phases was detected on the m-TiO_2*-reox support, indicating structural change of the support upon reoxidation. Whatever the support, A-TiO_2 crystallites (25±1 nm) are smaller than those of R-TiO_2 (30-45 nm). Similar crystallite sizes were reported by other authors for TiO_2 P25 [35, 36]. The A-TiO_2, but above all, the R-TiO_2 crystallite sizes decrease upon reduction (m-TiO_2* and d-TiO_2*) and increase again upon reoxidation (m-TiO_2*-reox). The decrease of R-TiO_2 crystallite size can be associated to the formation of an amorphous or disordered layer of reduced TiO_2 around a crystallite core, resulting in the formation of a crystalline-disordered core-shell structure [21]. Therefore, the R-TiO_2 phase is the most reactive one towards $NaBH_4$ reduction, and is mainly involved in the formation of a disordered TiO_2@TiO_{2-x} shell. Other authors reported similar results, with a preferential reduction of the R-TiO_2 over the A-TiO_2 phase due to longer Ti-O bonds in the rutile crystal structure [27, 37]. The decrease of R-TiO_2 crystallite size and the formation of an amorphous or disordered layer of reduced TiO_2 should also be associated to the increase of the surface area observed on the most reduced d-TiO_2* sample (Table S2).

XRD, EPR and Raman characterization show that reduction with $NaBH_4$, of TiO_2-P25 leads to the formation of defects (O_v, Ti^{3+}) and to the formation of new Na- and B-containing phases. It is mainly the most reactive R-TiO_2 phase which undergoes structural modification upon reduction. Upon reoxidation the O_v and Ti^{3+} defects disappear, letting behind the Na and B promoters.

H_2-temperature programmed reduction (H_2-TPR analyses) show that the reduction by hydrogen is moderate for all the supports (**Figure S3a** and **Table S2**), due to the presence of a large fraction of anatase phase [38]. TiO_2-P25 exhibited no H_2 consumption peak in the 50-500 °C range, since its reduction normally occurs at T > 600 °C. The Na-promoted samples show reduction events at lower temperatures (400-500 °C) that might be attributed to the reduction of sodium species [39, 40].

The CO_2-temperature programmed desorption (CO_2-TPD) results show that the three modified supports can adsorb more CO_2, compared to the commercial TiO_2-P25 (**Figure S3b** and **Table S2**). The negligible difference between m-TiO_2* and m-TiO_2*-reox supports suggests that the increased basicity of the d-TiO_2* arises mainly from the presence of the promoters rather than from surface defects. Overall, the d-TiO_2* support, rich in both surface defects and promoters,

shows the highest basicity, which can contribute to an increase of CO_2 adsorption [6]. Since alkali metals can strongly promote CO_2 adsorption [40-42], we mainly attributed the increase in the basicity of the modified supports to the presence of Na (see **Figure S4** for the correlation between the amount of adsorbed CO_2 and the Na wt % in the different supports). Indeed, the basicity of Na-promoted Pt/TiO_2 catalysts has been attributed mainly to the presence of NaO_x species [40], and sodium titanate nanotubes have been identified as promising CO_2 adsorbents showing higher efficiency than the parent TiO_2 [43]. The CO_2-TPD profiles show also that the commercial TiO_2-P25 can only bond some CO_2 with a medium strength. Upon reduction, m-TiO_2* shows increased adsorption in both weak and medium strength ranges, and a small tail in the strong adsorption range. The latter becomes more significant on m-TiO_2*-reox support, indicating that the reoxidation might lead to the creation of new sites, which can strongly bond CO_2. Finally, the d-TiO_2* displays an important increase in the weak-medium bonded CO_2, and a very small tail in the strong-bonded range.
To summarize the support characterization results, the reduction of TiO_2 by $NaBH_4$ is a suitable one-step procedure to obtain partially reduced supports containing defects (O_v and Ti^{3+}) and Na and B promoters identified as crystalline phases, which can significantly increase CO_2 adsorption. The reoxidation of the m-TiO_2* support eliminates the surface defects, while conserving the promoters.

2.2 Co/x-TiO_2 catalysts. To investigate the effect of the different supports and their properties on CO_2-FTS performances, four cobalt based catalysts with 10 wt% Co (nominal loading) were prepared by IWI method. The catalysts and their real metal loadings (ICP-OES) are listed in the **Table 2**. Cobalt metal loadings were very close to their nominal value, as expected for the IWI synthesis. Cobalt species were observed on all calcined catalysts by Raman spectroscopy, notably in the form of Co_3O_4, which disappeared after reduction (*vide infra*). The crystallite size of Co_3O_4 (**Table 2**) was determined from the diffractograms of the calcined catalysts (**Figure S5**). Bulk characterization methods such as magnetic measurements and XRD show the presence of mainly metallic cobalt in all reduced samples (**Figure S5**). The measurement of the sample magnetization as a function of the applied magnetic field by vibrating-sample magnetometry (VSM) allows the determination of the saturation magnetization (M_s) of each sample (**Figure S5a**), which can be divided by the magnetization of bulk Co (M_s = 154 emu/g) to determine the percentage of metallic cobalt in each sample (**Table 2**).

Table 2. Real metal loading (ICP-OES) of the different catalysts of this study. Percentage of metallic Co (% Co^0) calculated from VSM measurements (300 K) in the reduced catalysts, and Co_3O_4 estimated crystallite size (from XRD on the calcined catalysts).

Catalyst	**ICP-OES (%wt)**			**% Co^0 (VSM)**	**Co_3O_4 (nm)**
	Co	Na	B		
Co/TiO_2	9.62	-	-	99.75	37.4
Co/m-TiO_2*	9.70	0.64	0.04	97.97	44.2

Co/d-TiO_2*	9.24	0.92	0.07	94.30	39.6
Co/m-TiO_2*-reox	9.88	0.47	0.02	91.44	38.1

The reduced Co/TiO_2 catalyst, which can be considered as the reference catalyst, contains the highest amount of metallic cobalt (99.75 %). This is in line with H_2-TPR, CO-TPD and diffuse reflectance infrared Fourier transform spectroscopy (DRIFT) characterizations (*vide infra*) that indicate a more difficult reduction, and probably the presence of some oxidized cobalt in the three promoted catalysts. Crystalline cobalt oxide was not detected by XRD on any of the reduced catalysts (**Figure S5b**), which contain only both *hcp* and *fcc* metallic Co. The crystallite sizes of a reduced 15 wt% FTS Co/TiO_2-P25 catalyst were measured by XRD (MoK_α radiation) to be approximately 20 nm for the *fcc* phase and a 2.5 nm for the *hcp* phase [44]. In our case (CoK_α radiation), due to the overlapping of several crystallographic phases, the quantification and crystallite size determination of the metallic Co was not conclusive. The percentages of the R-TiO_2 phase as well as the R-TiO_2 crystallite size in the four catalysts (**Table S3**) are similar, contrarily to the situation of bare supports (**Table S1**). To investigate whether the re-crystallization of the R-TiO_2 phase took place during the calcination or reduction steps, we followed its evolution during catalyst preparation (**Figure S6**). The results show that the re-crystallization takes place during the calcination step, that is, when the cobalt nitrate decomposition leads to the formation of a NO_x-rich highly oxidative environment [45]. Moreover, no peaks related to Na or B containing phases are visible on the XRD diagrams of the calcined or reduced catalysts, pointing toward an amorphization phenomenon. It was reported that $Na_2B_4O_7.5H_2O$ and $Na_{0.23}TiO_2$ can be removed from reduced TiO_2 *via* HCl washing, due to their instability in acid [46]. Therefore, it is possible that such phases are partially leached by the acidic Co nitrate solution during the IWI and redispersed on the catalyst to form amorphous phases during the different calcination/reduction steps.

High Resolution Transmission Electron Microscopy (HRTEM), Scanning Transmission Electron Microscopy Energy Dispersive X-ray spectroscopy (STEM-EDX) and Scanning Transmission Electron Microscopy-High-Angle Annular Dark-Field (STEM-HAADF) analyses were performed on the four reduced catalysts to evaluate the Co particle size and their distribution on the support. Due to the low contrast difference between Ti and Co atoms, the identification of Co particles requires constant EDX analysis. Moreover, the extended agglomeration and the broad size distribution of Co, which is present both as small and large particles (**Figure S7**), makes impossible an accurate evaluation of the Co particle size distribution. Evidence of the SMSI encapsulation effect was probed by STEM-HAADF. **Figures S8 to S11** show the presence of encapsulation and fringes/striations resulting from non-epitaxial growth between the metal and the support in the four catalysts [47-49]. EDX analyses on isolated Co particles confirm the presence of TiO_2 in the outmost encapsulation layer, which seems to be in part amorphous and in part crystalline. The formation of such layers is generally related to partial reduction of TiO_2 under reducing atmosphere [50], which is enhanced in the presence of metal thanks to hydrogen spillover [51]. SMSI is widely assumed to be due to migration of unstable TiO_x species onto the metal surface forming metal particles encapsulated by a TiO_x layers [12]. The encapsulation of Co particles by TiO_2 was confirmed on the Co/m-TiO_2*-reox catalyst by fast Fourier transform (FFT) analysis of STEM-HAADF micrographs.

A selected example of an isolated from the rest of the support Co particle is shown in **Figure 2**.

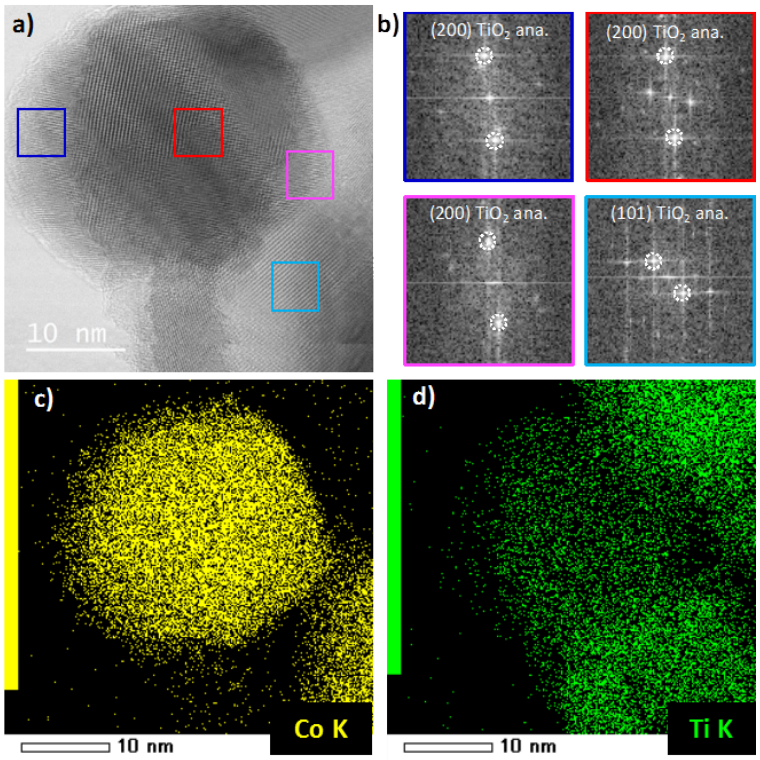

Figure 2. STEM-HAADF micrographs: **a)** bright field image; **b)** FFT patterns of the area framed with rectangles of corresponding colors, on which diffraction spots of the anatase phase are marked by dotted circles; **c)** and **d)** EDX mapping with Co (**c**, yellow) and Ti (**d**, green) of the Co/m-TiO_2*-reox catalyst.

The FFT patterns of the framed areas on **Figure 2a** are presented on **Figure 2b**. The Co and Ti EDX mapping are given in **Figures 2c** and **2d**. Both elements are present in the particle. The spots surrounded by dotted circles on **Figure 2b** were attributed to the (200) reflection of A-TiO_2. This reflection is observed throughout the particle (frames dark blue, red and magenta). For the particle in the bottom right-hand corner, A-TiO_2 is evidenced by the (101) reflection showing a different crystallographic orientation. The SMSI effect appearing during H_2 reduction has been shown to be more pronounced on Co/A-TiO_2 compared to Co/R-TiO_2 [52]. It is worth noting that this SMSI effect may be partly reversed during FTS, especially at high conversion [53]. Standard EDX is not appropriate for detecting light elements ($Z < 11$). Thus, boron cannot be detected by EDX, while the detection of Na is not easy due to its low Z (11), and its low concentration in all promoted catalysts. Sodium was detected on the Co/d-TiO_2* catalyst (**Figure S12**). Its location (on the support or on Co particles), cannot be precisely determined, as most of the time Co and TiO_2 particles overlap. However, some analyses on isolated Co particles have revealed association of Na, Ti and Co. For the Co/m-TiO_2* (**Figure S13**) and Co/m-TiO_2*-reox (**Figure S14**) catalysts, Na seems to be associated to the support.

The presence of radical species on the calcined catalysts was probed by EPR (**Figure S15**). Their concentration is extremely low (<1 nmol/mg) on all the catalysts and few residual O_v are detectable only on the catalysts prepared on the promoted supports. Such residual species might

be related to defects in the subsurface layers, which are not re-oxidized, or simply, to the presence of Na and B, which doping favors the formation of O_v and Ti^{3+} [54]. The surface defects can, in theory, be reformed during the reduction step or during catalysis, for example thanks to hydrogen spillover [55-57]. EPR studies were attempted on the reduced catalysts to verify any further formation of surface defects. However, the presence of ferromagnetic Co^0 strongly perturbed the cavity, preventing us from collecting meaningful spectra.

To overcome this limitation of EPR, we followed by *in situ* Raman analysis the evolution of the TiO_2 bands during the reduction of the catalysts under H_2 at 340°C, as well as during reaction under CO_2/H_2 (1 bar) at 220 °C (**Figure S16**). On the calcined catalysts, the A-TiO_2 $E_g(1)$ band was initially at a lower position on Co/TiO_2 (*ca*. 146 cm^{-1}) than on the promoted catalysts (*ca*. 147-148 cm^{-1}). Since EPR analyses point to very few O_v and Ti^{3+} on the calcined catalysts, this shift should be associated to the disorder induced by the presence of dopants in the promoted catalysts [58]. In the course of the reduction, the band of Co/TiO_2 at *ca*. 146 cm^{-1} evolved, notably when cobalt oxide was reduced but it finally remained *ca*. 2 cm^{-1} lower than on the promoted catalysts. During the reaction with CO_2/H_2, the band on Co/TiO_2 stabilized at 144 cm^{-1} while the band for Co/m-TiO_2* and Co/m-TiO_2*-reox remained centered at *ca*. 148 cm^{-1}. These analyses do not support the formation of O_v and Ti^{3+} during the reduction of the catalysts or during reaction under 1 bar.

The surface state of the catalysts was analyzed by X-ray photoelectron spectroscopy (XPS). The samples were initially reduced at 400 °C under 7 mbar H_2 for 30 min in a variable pressure reactor attached to the spectrometer and then transferred under vacuum for the XPS measurements (*quasi in situ* XPS). The XPS survey scans (**Figure S17)** are dominated by the photoemission and Auger peaks of TiO_2 and Na (for promoted catalysts) in addition to carbon peak typically present on samples synthesized by chemical methods. The B 1s and Co 2p peaks are less visible in the survey scans indicating lower surface concentration. According to the high-resolution spectra shown in **Figure 3a**, the binding energy (BE) of the Ti $2p_{3/2}$ peak at 458.7(±0.2) eV (in parenthesis the variation among the different catalysts) corresponds to Ti^{4+} ions of stoichiometric TiO_2, while there are no evidences of Ti^{3+} presence, typically manifested at the low BE side of the Ti 2p peak [59].

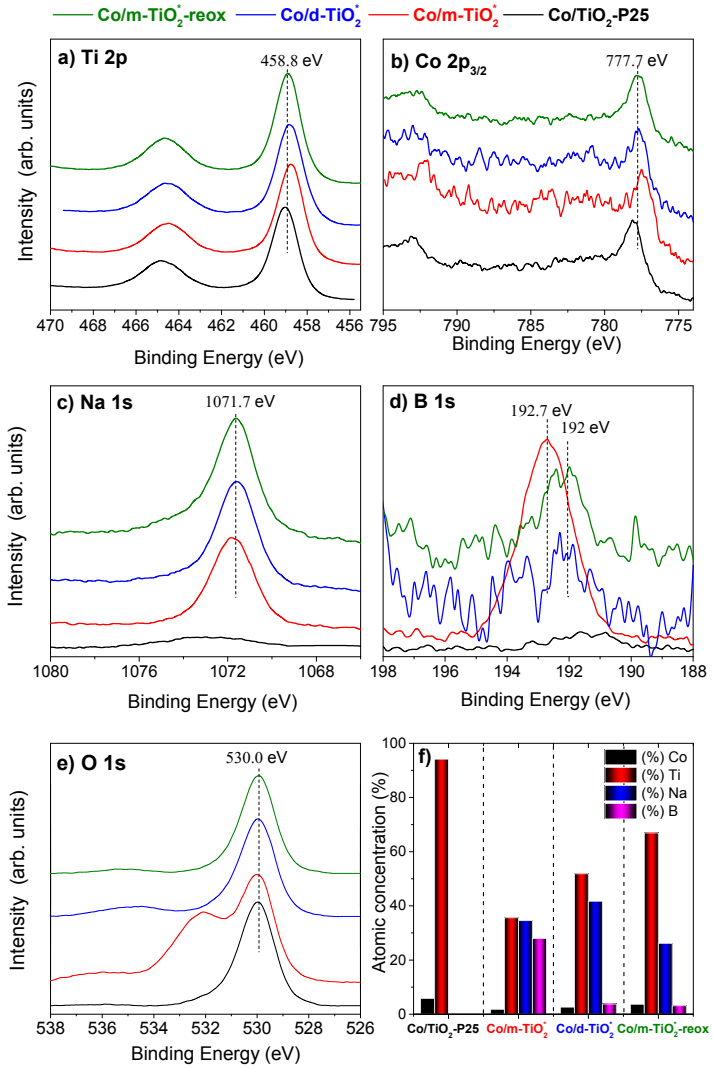

Figure 3. a) Ti 2p; **b)** Co $2p_{3/2}$; **c)** Na 1s; **d)** B 1s; **e)** O 1s *quasi in situ* X-ray photoelectron spectra measured after reduction at 400 °C in 7 mbar H_2 of Co/TiO_2^* (black line), $Co/m\text{-}TiO_2^*$ (red line), $Co/d\text{-}TiO_2^*$ (blue line) and $Co/m\text{-}TiO_2^*$-reox (green line) catalysts. All peaks are normalized to the same height. **f)** The surface atomic concentration of the four catalysts calculated by the *quasi in situ* XPS results.

The Co $2p_{3/2}$ peak at 777.7(±0.2) eV is characteristic of metallic Co (**Figure 3b**) [60, 61], but traces of ionic cobalt cannot be excluded due to the low signal to noise ratio. The BE of Na 1s for all promoted catalysts appear at 1071.7(±0.1) eV (**Figure 3c**). According to previous XPS studies, this BE is associated either to sodium (bi)carbonates [62, 63] or sodium-titanate compounds [64-66]. The formation of sodium oxides (e.g. Na_2O) or hydroxides (e.g. NaOH) is rather unlikely, since in this case the Na 1s appears either at higher or lower BEs, respectively than 1071.7 eV [67, 68]. The C 1s spectra can help to distinguish between sodium titanate and carbonate species since carbonates should be accompanied by a characteristic C 1s peak at around 290 eV [62]. As shown in **Figure S18**, the C 1s region is dominated by a component at 284.6±0.1 eV due to hydrocarbons, excluding carbonate formation. Based on that, we conclude that Na interacts with the TiO_2 support to form sodium-titanate. The B 1s peak of $Co/m\text{-}TiO_2^*$ is centered at 192.7±0.1 eV, while for the other two promoted samples it is around 192 eV and is significantly less intense (**Figure 3d**). Previous reports indicated that B 1s peak is sensitive to the local chemical environment of boron [69-72]. In particular, anionic B^{2-} (*i.e.* TiB_2 or CoB)

and cationic B^{3+} (*i.e.* B_2O_3) appears around 187.5 eV and 193 eV, respectively; while B occupying substitutional or interstitial TiO_2 sites is found between 190 and 192 eV [69-73]. Accordingly, on Co/m-TiO_2* surface boron forms an oxide (e.g. B_2O_3), while on Co/d-TiO_2* and Co/m-TiO_2*-reox it is most likely incorporated into TiO_2. The O 1s spectra (**Figure 3e**) are very similar for Co/TiO_2, Co/d-TiO_2* and Co/m-TiO_2*-reox catalysts, with a peak at 530.0(±0.1) eV ascribed to lattice TiO_2 species [74]. A distinctly different spectrum is found for Co/m-TiO_2*, with an additional O 1s component around 532.3 eV, typically attributed to hydroxyl groups [74]. For the Co/m-TiO_2* catalyst, this peak can be also related to boron oxide [74]. Calculation of the boron oxide stoichiometry by the O 1s and B 1s spectra, assuming that the component at 532.3 eV is exclusively related to boron oxide, gives a stoichiometry of $BO_{2.2}$, which is significantly higher than the one expected for common boron oxides (*i.e.* boron trioxide, $BO_{1.5}$). Based on this, one can safely assume that apart of boron oxide, a significant population of OH groups is stabilized on Co/m-TiO_2*.

The intensity of the XPS spectra allows quantifying the concentration of the chemical elements on the surface. As shown in **Figure 3f**, the Co surface concentration (in at. %) is below 6 % for all catalysts, which is significantly lower than the bulk concentration measured by ICP-OES (**Table 2**). Taking into account the surface sensitivity of XPS (estimated analysis depth *ca.* 7 nm), this result suggests encapsulation of Co under TiO_2 as shown by STEM-HAADF analyses. Notably, the lowest cobalt concentration was measured on Co/m-TiO_2* (around 2%) and the highest on Co/TiO_2 (around 6%). The reason for the presence of a greater quantity of boron on the surface of Co/m-TiO_2* compared to the other two promoted catalysts is still unclear. The concentration of Na promoter is several hundred times higher on the surface than in the bulk (**Table 2**), indicating it is preferentially located on the surface. The trend in Na concentration is qualitatively similar with the ICP-OES measurements shown in **Table 2**. Overall, XPS analyses give critical information regarding the surface chemical state, and notably on the nature of the promoters. The Co/d-TiO_2* catalyst shows the highest surface concentration of Na among the catalysts and the Co/m-TiO_2* presents a high amount of B on its surface. Boron exists as an oxide or is incorporated into TiO_2, while Na interacts with TiO_2 as sodium-titanate. Finally, the surface concentration of cobalt is lower than in the bulk, confirming spillover of TiO_2.

The local geometric and electronic structure of cobalt was further analyzed by hard X-rays Absorption Spectroscopy in X-ray Absorption Near Edge Structure (XANES) and Extended X-Ray Absorption Fine Structure (EXAFS) regions. *Ex-situ* Co K-edge spectra of the four reduced catalysts recorded after air exposure, together with reference spectra of CoO and metallic Co (foil), are shown in **Figure 4a**. For all catalysts, the spectrum line shape corresponds to a mixture of Co and CoO phases indicating partial cobalt oxidation, as expected for Co/TiO_2 catalysts exposed to the air [75]. The Co K-edge of the Co/TiO_2 catalyst is different from the other three, showing a clear decrease of the shoulder in the rising edge combined with increased whiteline intensity. Differences are also observed in the Fourier-transformed (FT) EXAFS (**Figure 4b**) with a less intense Co-Co scattering path in the second shell as compared to the other samples due to lower metal concentration. Linear combination analysis (LCA) of the XANES region (**Figure S19**) confirms the higher CoO fraction in Co/TiO_2 due to air exposure. Fit of FT-EXAFS spectra (**Figure S20**) was conducted to gain more insights on cobalt local structure. Due to the intrinsic correlation between Co species concentration, coordination number (CN) and Debye Waller (DW) factor to the dampening of shell intensity, reasonable constrains were applied. Indeed, species concentration was fixed to LCA results and CN was constrained to crystallographic values, while only DW factors were fit as free variables. The obtained DW factors (**Table S4**) are all physically correct, indicating that the employed CN were suitable to describe the presence of CoO and metallic Co. Thus, for all catalysts the majority of cobalt particles have bulk characteristics, which are generally attained for sizes

above 3 nm [76, 77]. Apart from the particle size, the radial Co-Co distance is sensitive to potential interaction of cobalt atoms with heteroatoms. As shown in **Table S4**, the radial distances in the first and second cell are identical with those of bulk Co and CoO phases, which rule out the possibility of Co-Ti, Co-B or Co-Na compounds formation.

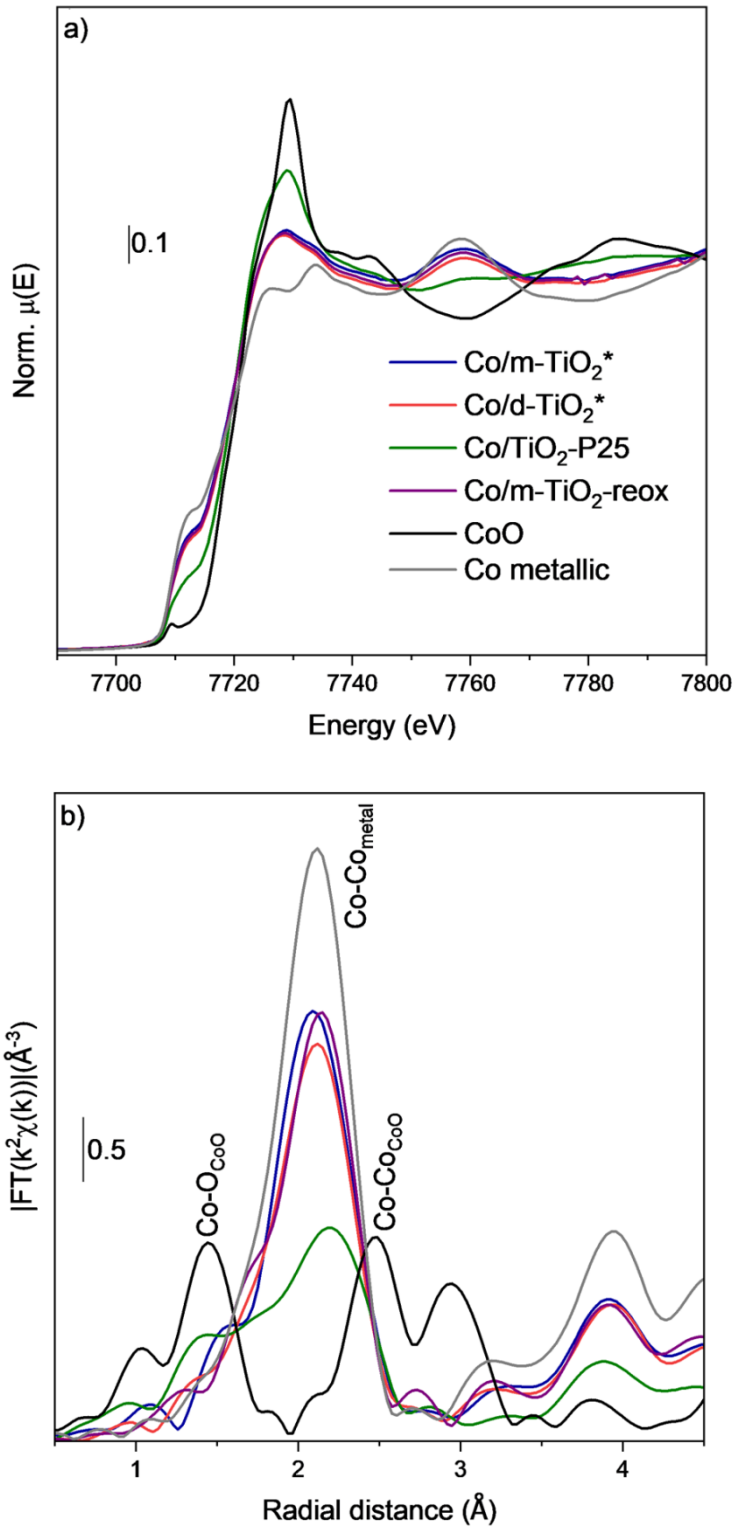

Figure 4. Co K-edge XANES **a)** and **b)** FT-EXAFS spectra collected *ex situ* on reduced Co/m-TiO_2 (blue line), Co/d-TiO_2* (red line), Co/TiO_2 (green line) and Co/m-TiO_2*-reox (purple

line) catalysts. Reference spectra of CoO (black line) and metallic Co (grey line) are reported for clarity. Experimental EXAFS spectra are reported in **Figure S19** for clarity.

However, due to the relatively large cobalt particles, the EXAFS spectra in our case are not sensitive to surface or interface interactions, therefore one cannot exclude that cobalt is in contact with Na or B, but we can only talk about two separate phases. Overall, EXAFS analysis indicates that cobalt electronic and geometric structure of all examined catalysts is very similar with particle exceeding 3 nm, and the absence of mixed Co-B or Co-Na compounds.
To summarize catalyst characterization results, high levels of cobalt reduction (> 90%) have been obtained for the four reduced catalysts, and no specific charge transfer between cobalt and support or promoters is evidenced from XPS. SMSI encapsulation effect was evidenced for the four catalysts by STEM-HAADF and confirmed by XPS. After cobalt deposition on the modified TiO_2 supports, the defects (O_v and Ti^{3+}) present on the bare supports disappear due to the highly oxidative atmosphere present during the calcination step. XPS and *in situ* Raman analyses support the fact that these defects did not reappear upon catalyst reduction. The promoters (Na and B) are present on the surface of promoted catalysts. Sodium, which is the main promoter, is mainly present as an amorphous sodium-titanate phase. Boron is present in lower amounts than Na, and exists as an oxide or is incorporated into TiO_2. The cobalt electronic/geometric structure of the four catalysts is very similar, and did not include mixed Co-B or Co-Na compounds.

2.3 CO_2-FTS on Co/TiO_2 catalysts. The catalytic results at T = 220 °C after 50 h on stream are presented in **Table 3** and **Figure 5**. The catalyst prepared on TiO_2-P25 shows, as expected [78], a very high selectivity of 93 % towards methane. The three catalysts prepared on the modified supports display significantly higher selectivity towards C_{2+} and C_{5+} products. Overall, the catalysts prepared on the reduced supports, namely Co/m-TiO_2* and Co/d-TiO_2* present the lowest Y_{CH4} and the highest Y_{C2+} and Y_{C5+}.

Table 0. X_{H2}/X_{CO2} ratio, and yields ($mol_Z \cdot mol_{Me}^{-1} \cdot h^{-1}$, Z = CH_4, C_{2+}, CO) of the catalysts after 50 h on stream at T = 220 °C, P = 20 bar, H_2/CO_2 = 2, WHSV = 1620 $mL \cdot g_{cat}^{-1} \cdot h^{-1}$.

Catalyst	**CO_2 conversion (%)**	**X_{H2}/X_{CO2}**	**Y_{CH4}**	**Y_{C2+}**	**Y_{CO}**
			($mol_Z \cdot mol_{Me}^{-1} \cdot h^{-1}$)		
Co/TiO_2	26	1.73	3.22	0.23	0.00
Co/m-TiO_2*	28.1	1.61	2.31	1.36	0.01
Co/d-TiO_2*	15.9	1.56	1.26	0.95	0.02

Co/m-TiO_2*-reox	31.4	1.68	3.09	1.01	0.01

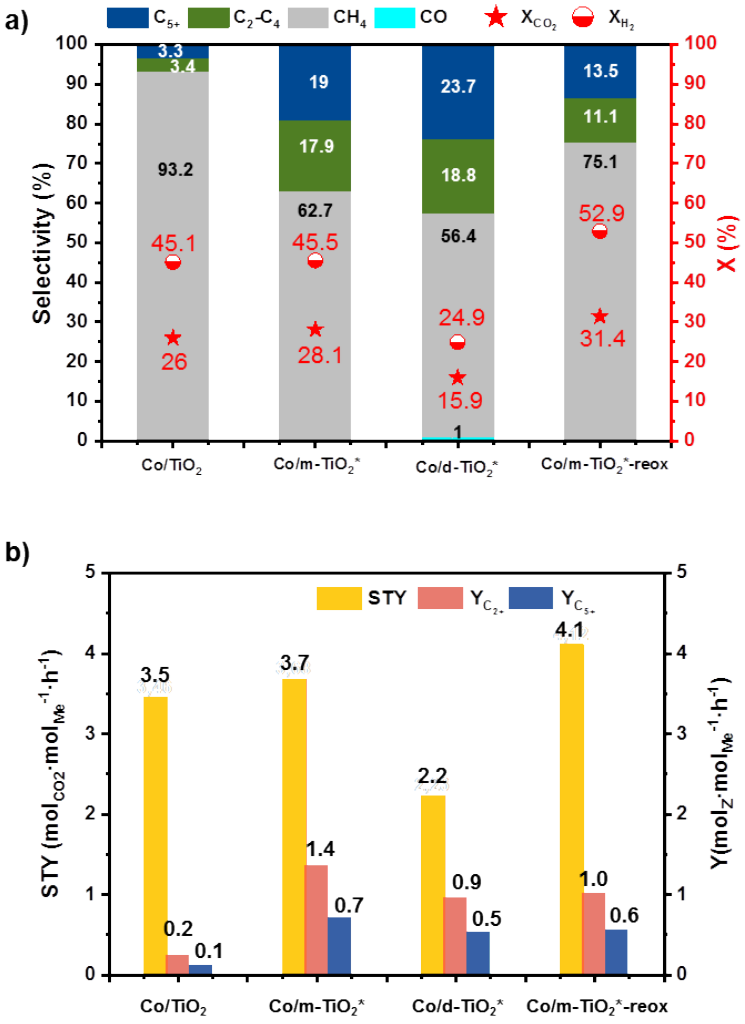

Figure 5. a) Conversion (red) and selectivity (black or white); **b)** Space-time yield (STY, $mol_{CO2}·mol_{Me}^{-1}·h^{-1}$) and yields (Y, $mol_Z·mol_{Me}^{-1}·h^{-1}$, Z = C_{2+}, C_{5+}) of the catalysts involved in this study after 50 h on stream, T = 220 °C, P = 20 bar, H_2/CO_2 = 2, WHSV = 1620 $mL·g_{cat}^{-1}·h^{-1}$.

Few amounts of CO are formed on the catalysts prepared from modified supports. The lower X_{H2}/X_{CO2} ratios of the modified catalysts (**Table 3**), may indicate a lower surface H/C coverage. Several authors have reported that a low H/C coverage allows limiting methanation and enhancing RWGS activity, which in turn promotes chain growth [6, 78]. As far as CO_2 conversion is concerned, it is significantly reduced for the Co/d-TiO_2* catalyst, which contains the higher sodium concentration. The presence of promoters in smaller concentrations on Co/m-TiO_2* and Co/m-TiO_2*-reox catalysts did not affect the CO_2 conversion. At 220 °C, Co/m-TiO_2* is the best catalyst for C_{2+} production.

A series of tests was also performed for 25 h at 250 °C and 20 bar, after the initial tests at 220 °C, which are presented in **Table 4** and **Figure 6**.

Table 4. X_{H2}/X_{CO2} ratio after 25 h on stream; yields ($mol_Z \cdot mol_{Me}^{-1} \cdot h^{-1}$, Z = CH_4, C_{2+}, CO) of the catalysts involved in this study after 25 h on stream at T = 250 °C, P = 20 bar, WHSV = 1620 $mL \cdot g_{cat}^{-1} \cdot h^{-1}$.

Catalyst	CO_2 conversion (%)	X_{H2}/X_{CO2}	Y_{CH4}	Y_{C2+}	Y_{CO}
			($mol_Z \cdot mol_{Me}^{-1} \cdot h^{-1}$)		
Co/TiO_2-P25	43.8	1.77	5.49	0.33	0.01
Co/m-TiO_2*	42.7	1.64	3.69	1.88	0.02
Co/d-TiO_2*	34.9	1.58	2.48	2.30	0.05
Co/m-TiO_2*-reox	44.7	1.75	4.77	1.07	0.02

At 250 °C, all catalysts are more active than at 220 °C; and several differences can be noticed in the product distribution. First, the selectivity towards CH_4 increases on most catalysts, because of a higher H_2 activation level revealed also by an increase of the X_{H2}/X_{CO2} ratio (**Table 4**). Moreover, the selectivity towards C_2-C_4 products increases at the expense of C_{5+}. The only catalyst that does not follow this trend is Co/d-TiO_2*. This catalyst produces slightly less CH_4 and more C_2-C_4 products at 250 °C than at 220 °C. Consequently, Co/d-TiO_2* is the best catalyst at 250 °C, showing even higher Y_{C2+} ad Y_{C5+} than Co/m-TiO_2*. The presence of a higher amount of promoter on Co/d-TiO_2* likely permits to maintain a good H/C surface ratio at 250 °C, similarly to what occurs on other alkali promoted catalysts [16, 41, 79, 80]. Therefore, Co/m-TiO_2* and Co/d-TiO_2* are the best catalysts to produce C_{2+} and C_{5+} *via* CO_2-FTS, at 220 °C and 250 °C, respectively. Although it is difficult to compare the catalytic performance of different systems reported in the literature due to the use of different reactors and often not strictly identical operating conditions, the two catalysts Co/m-TiO_2* and Co/d-TiO_2* performed very well in terms of STY and in particularly of Y_{C2+} compared to the best cobalt catalysts described in the literature for CO_2-FTS (**Table S5**).

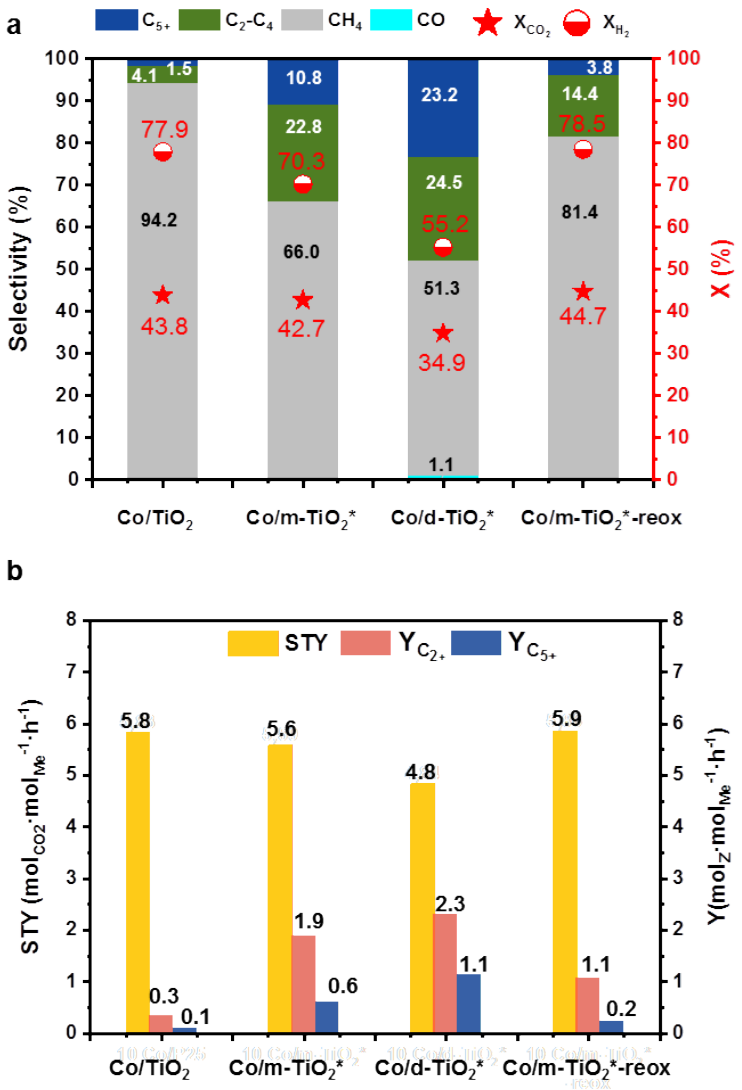

Figure 6. a) Conversion (red) and selectivity (black or white); **b)** STY ($mol_{CO2}·mol_{Me}^{-1}·h^{-1}$) and yields ($mol_Z·mol_{Me}^{-1}·h^{-1}$, Z = C_{2+}, C_{5+}) of the catalysts involved in this study after 25 h on stream, T = 250 °C, P = 20 bar, H_2/CO_2 = 2, WHSV = 1620 $mL·g_{cat}^{-1}·h^{-1}$.

To investigate any modification of the catalyst structure during the reaction, XRD was performed on the four catalysts after catalytic tests at 250 °C. XRD diffractograms of the spent catalysts are shown in **Figure S21**, and the main parameters of the TiO_2 phases are summarized in **Table S6**. XRD patterns of the used catalysts show the presence of a sharp peak, centered at 30.9°, which is attributed to graphitic carbon (**Figure S21a**) [44]. Small variations of the *hcp*- and *fcc*-Co peaks suggest modifications of the Co active phase during the catalytic tests. The formation of cobalt carbides can be envisaged [81]. The most intense peak of Co_3C should be centered at ~ 51.7°, and is overlapped with other phases. Isolated diffraction peaks of Co_3C with lower intensity are not visible. However, the presence of this phase cannot be completely excluded. No significant variation of anatase and rutile crystallite size, or rutile phase percentage was noticed after catalysis (**Table S6** and **Table S3**).

According to **Table S5**, Co/m-TiO_2* and Co/d-TiO_2* have been identified as the most performing catalysts. To assess their stability and collect some oil products for α determination,

long tests were performed at 220 °C and the results are presented in **Figure S22** and **Figure S23**. The Co/m-TiO_2* catalyst (**Figure S22**) is extremely stable at 20 bar and 220 °C, while Co/d-TiO_2* catalyst (**Figure S23)** shows a fluctuating behavior, needing 75-100 h on stream for its performance to be stabilized. These, and other similar tests carried out at both 220 and 250 °C on these two catalysts allowed the collection of liquid hydrocarbons as illustrated in **Figure S24**. For GC analysis, three different CO_2-FTS catalytic tests, which produced the highest amount of oil products, were considered (**Table S7**). The oil fractions were analyzed by GC-SimDist. **Figure 7** shows the product distribution of the oil phase as a function of carbon chain length (n) and corresponding chain growth probability (α). No alcohols were detected in the water fractions by GC and GC-MS. No C_2H_4 was detected during the catalytic tests with any of the four catalysts involved in this study. The results of the SimDist analysis show that the C_{5+} products for both catalysts correspond mainly to the jet-fuel fraction (C_8-C_{16}), with only a small difference between the two catalysts. Consequently, the α values are very similar between these two catalysts, and are close to the maximum values that can be obtained in CO_2-FTS (0.5-0.6) [82-84]. Slightly higher α value was obtained during the single test at 220 °C on the Co/d-TiO_2* catalyst, indicating that 220 °C is a more suitable temperature for CO_2-FTS, and an increase in the operating temperature favors chain termination, which is in line with the observed variation of selectivity. However, we must take into consideration that the α variations of these three different tests might be related to the different time on stream (TOS) at 220 °C and 250 °C.

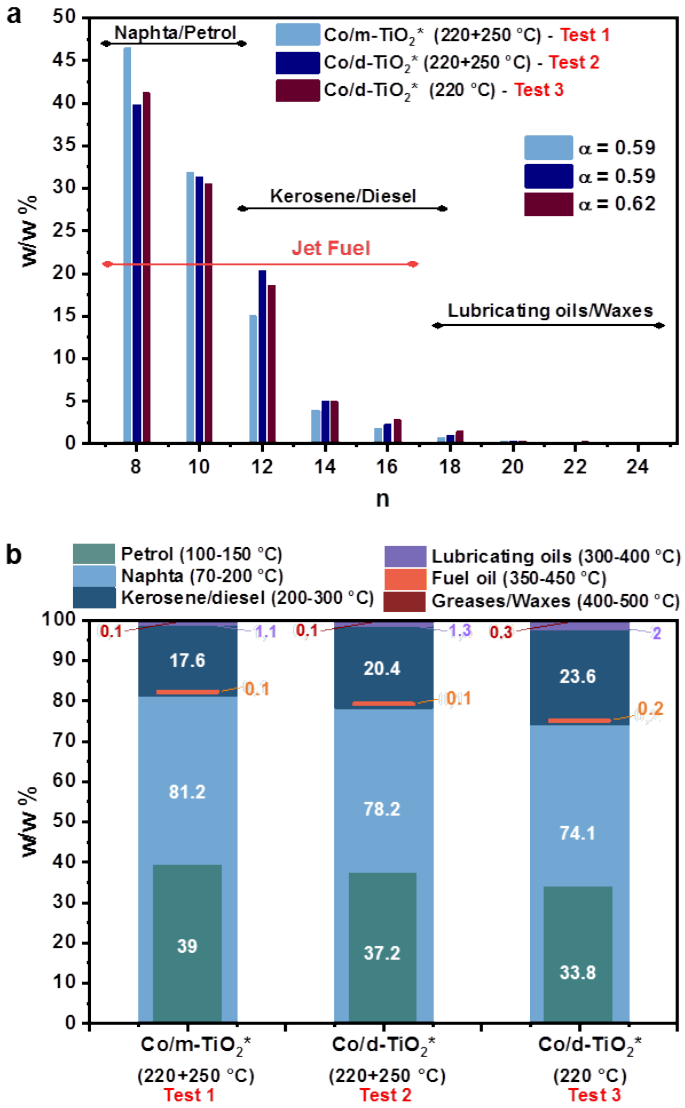

Figure 7. a) Product distribution of the oil liquid phase as a function of carbon chain length (n) and corresponding chain growth probability (α). Light blue = Test 1: catalyst Co/m-TiO_2*, 150 h at 220 °C + 50 h at 250 °C; Test 2: dark blue = catalyst Co/d-TiO_2*, 70 h 220 °C + 70 h at 250 °C; Test 3: wine = catalyst Co/d-TiO_2*, 225 h at 220 °C; P = 20 bar, H_2/CO_2 = 2, WHSV = 1620 $mL \cdot g_{cat}^{-1} \cdot h^{-1}$. **b)** Product distribution of the oil liquid phases expressed in terms of different distillation fractions.

2.4 Impact of TiO_2 modification on CO_2-FTS and structure/performance correlation. To rationalize the obtained catalytic results and try to correlate the catalyst performance to their structure, additional characterizations were performed on the four catalysts.

CO_2-TPD, CO-TPD, N_2 adsorption isotherm and H_2-TPR analyses are shown in **Figure S25**, and the main results are summarized in **Table S8**. The catalysts prepared on the modified supports, although presenting a similar specific surface area as Co/TiO_2, adsorb higher amount of CO_2 than Co/TiO_2. All Co-based catalysts adsorb less CO_2 than the corresponding bare supports (**Figure S26**). Such result indicates that the support plays a major role in CO_2 adsorption [40], and Co particle deposition should induce the blocking of part of the CO_2

adsorption sites of the supports. This phenomenon is much less pronounced for the Co/m-TiO_2*-reox sample. This might be related to a different distribution of Co particles, a different extent of SMSI, or to the presence of different CO_2 adsorption sites on this catalyst, resulting from a different location of the promoters on the support, probably related to surface reconstruction during the reoxidation step. The total amounts of adsorbed CO_2 cannot be directly correlated to the STY or selectivity of the catalysts. If we consider only the medium/strongly adsorbed CO_2 on the various catalysts, notable differences are observed between the four catalysts (**Figure S27**). Particularly, the more active Co/m-TiO_2*-reox catalyst shows the highest amounts of the medium/strongly adsorbed CO_2 and the opposite is observed for the less active Co/d-TiO_2* catalyst. The reason why this latter catalyst shows the lower amount of medium/strongly adsorbed CO_2 is still unclear. If we now consider this amount of medium/strongly adsorbed CO_2, which should be important for the catalytic reaction, it correlates well with catalyst activity (**Figure 8a**), but not with selectivity. At a first glance, it might be surprising that the Co/d-TiO_2* catalyst, which present the higher sodium loading and the higher surface Na concentration, is the less active. However, beside CO_2 activation *via* adsorption, promoters can play different roles in the reaction. For instance, it was reported that small amount of B (< 0.1%) can decrease the H_2 uptake of a 10 wt% Co/TiO_2 catalyst, and increase the final α during traditional CO-FTS [85]. Alkali metals are electron donors and, therefore, may act by enhancing chemisorption of electron acceptor species, such as CO,[86] and/or by suppressing chemisorption of electron donors, such as H_2 [87]. The electron donation from the alkali promoters to the metal species, results in a decreased possibility of electron donation from H_2, thus, limiting its activation [16, 41]. Such phenomena have already been reported for Na_2O-doped Co catalysts [88, 89]. The lower STY (2.2 $mol_{CO_2}.mol_{Co}^{-1}.h^{-1}$) obtained for the Co/d-$TiO_2$* catalyst, might be related to strong electronic interactions between Co sites and the promoter(s). Such interaction strongly limits H_2 activation, resulting in a reduced activity, but good selectivity. For the other modified catalysts, the STY varied between 3.4 and 4.1 $mol_{CO_2}.mol_{Co}^{-1}.h^{-1}$ for Co/TiO_2 and Co/m-TiO_2*-reox, respectively. It is therefore unlikely that Na interacts significantly with cobalt in these two catalysts, which are significantly more active than the Co/d-TiO_2* catalyst. Therefore, the promoter(s) should be on the support, and available for CO_2 activation. We independently prepared a Co-1%Na/m-TiO_2* catalyst, obtained by the addition of 1 wt% Na to the Co/m-TiO_2* by IWI method using $NaNO_3$ as precursor. In this new catalyst, it is likely that the excess promoter can also deposit on the metal. The Co-1%Na/m-TiO_2* catalyst shows a drastic decrease of the activity, but not of the selectivity, in comparison with Co/m-TiO_2* (**Figure S28**).

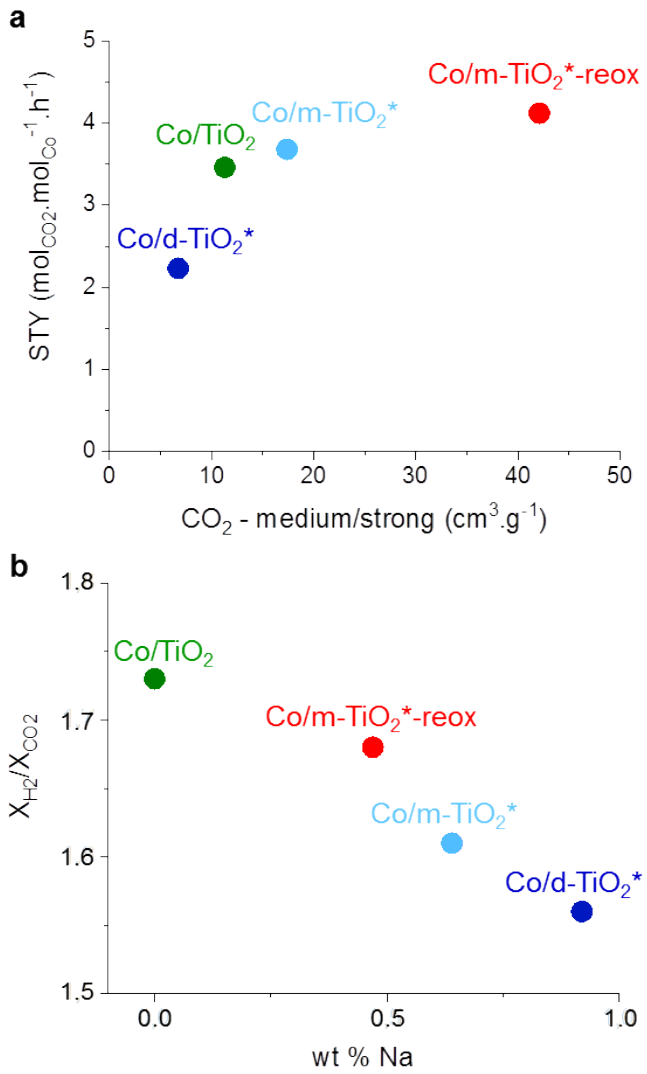

Figure 8. a) Evolution of STY (based on total Co) with the amount of CO_2 adsorbed medium/strongly on the catalyst surfaces; and **b)** evolution of the X_{H2}/X_{CO2} ratio during CO_2-FTS and the sodium loading in the catalysts.

Therefore, it is reasonable to propose that when Na is directly interacting with cobalt in the modified catalysts (located on cobalt or at perimetric sites of Co crystallites) [87], its presence strongly decreases catalyst activity and increases its selectivity compared to the unpromoted catalyst. This is the case of the Co/d-TiO_2* catalyst, for which, interestingly, Na and Co were detected on the same areas (**Figure S12**). Alternatively, when Na is present mainly on the support of modified catalysts (added alkalis interact strongly with the TiO_2 surface) [54], its presence does not affect catalyst activity, but only its selectivity as compared to unpromoted catalyst. This is a key result of this study, which will be discussed in more detail later. Globally, we found that the amount of sodium in the catalyst impacts the X_{H2}/X_{CO2} ratio; the higher the Na loading, the lower is this ratio (**Figure 8b**).

We can have an idea about H_2 activation on these catalysts from H_2-TPR profiles (**Figure S25b**). All catalysts display the main reduction events in a temperature range between ~ 300-600 °C, attributed mainly to the reduction of Co_3O_4 to CoO and CoO to metallic Co. Differences can be observed in the shapes of the profiles, which might be related to different Co particle size distributions (smaller Co particles have been reported to be more easily reduced on TiO_2 [90]) and/or different interactions with the support or promoter. The Co/TiO_2 catalyst shows

the easiest reduction, which starts slowly at low temperature (*ca.* 120 °C). On Co/m-TiO_2*, the reduction starts at slightly higher temperature (*ca.* 150 °C). The different shape of the reduction peaks between Co/m-TiO_2* and Co/m-TiO_2*-reox suggests a different interaction between cobalt and the support in these two catalysts showing similar amounts of promoters (**Table 1**). This was confirmed by Raman analyses (*vide infra*). The Co/m-TiO_2*-reox catalyst shows the lower H_2 consumption of the series. On Co/d-TiO_2*, the reduction starts at higher temperature (*ca.* 300 °C) and also finishes at higher temperatures than on Co/TiO_2, indicating a more difficult reduction. This should be associated to the interaction between the promoter and the metal, which can limit H_2 activation and inhibit the reduction of the active phase [91, 92]. It was also shown that the presence of R-TiO_2, which is the lowest for the Co/d-TiO_2* catalyst (**Table S6**), can facilitate the reduction process of cobalt oxide species on TiO_2 [93]. **Figure S29** shows that globally, the quantification of TPR results (H_2 consumption, **Table S8**) is in line with the VSM results (**Table 2**). At that point, it is interesting to notice that neither the catalyst activity nor their selectivity can be correlated to the reduction degree of cobalt.

Reduction of the Co/TiO_2, Co/m-TiO_2* and Co/m-TiO_2*-reox catalysts was also followed by *in situ* Raman spectroscopy (**Figure S30**). Before treatment, Co/TiO_2 and Co/m-TiO_2*-reox clearly showed well-defined bands at 469, 510 and 678 cm^{-1} attributed to the spinel Co_3O_4 phase [52]. On both solids, heating under dihydrogen leads to a progressive decrease of these bands already above 60 °C and more pronounced above 120 °C. Above 250 °C, the bands of cobalt oxide become too weak to be detected. Interestingly, different bands appear on the Co/m-TiO_2* sample, where a broad peak is observed at 681 cm^{-1} and smaller bands at lower wavenumbers. These bands, which are easier to observe when the contribution of TiO_2 is subtracted (**Figure S30b**), get better defined up to 110 °C where the main band also shifts to 686 cm^{-1} and the smaller bands are observed at 227, 260, 329, 379, 427 and 602 cm^{-1}. These bands are consistent with those reported for the ilmenite $CoTiO_3$ phase [94, 95]. After this preliminary transformation, heating induces a first transformation to Co_3O_4, as observed on the other solids, and its progressive reduction. After reduction, all solids finally showed only the spectrum of TiO_2 and the disappearance of the cobalt oxides, confirming their complete reduction to metallic cobalt. The low temperatures at which changes are observed probably indicate a good initial dispersion of the cobalt species.

The CO-TPD analyses (**Figure S25c** and **Table S8**) indicate that all the catalysts adsorb moderate amounts of CO compared to CO_2. The CO-TPD profiles show that the promoted catalysts adsorb most of the CO with a weaker bonding than Co/TiO_2. We also noticed that among the promoted catalysts, a higher amount of medium bonding CO is observed for the Co/d-TiO_2* catalyst, which can suggest direct interaction between Na and Co [86]. The stronger CO bonding on Co/TiO_2, along with the availability of a high number of H species, might favor its immediate hydrogenation to CH_4. *Operando* DRIFT analyses have been carried out on catalysts Co/TiO_2, Co/m-TiO_2* and Co/d-TiO_2* to probe adsorbed CO and CO_2 species. The results are shown in **Figure 9a**.

At 220 °C, 1 bar and H_2/CO_2 = 2, the principal surface species are quite different between the unpromoted and promoted catalysts. Only bands at 2964, 2880, 1562 and 1366 cm^{-1}, which are assigned to formate species adsorbed on titania, are present on the Co/TiO_2 catalyst. The corresponding vibration modes are detailed elsewhere [96]. Additional bands were observed in the case of the promoted samples, which could correspond to sodium formates [97, 98] and carbonates [99, 100]. It has been reported that for unpromoted Co/TiO_2 catalysts, the CO_2 hydrogenation reaction proceeds through formate species on Co/R-TiO_2 (which is further converted to CH_4), while Co/A-TiO_2 undergoes $CO_2 \rightarrow$ *CO (which desorbs to form gas-phase CO instead of subsequent hydrogenation) [16]. The formation of carbonate species on the promoted catalysts could be related to the presence of Na [43, 101]. Interestingly, under H_2/CO

= 40 (**Figure 9b**), only the Co/TiO_2 catalyst, which presents the highest surface cobalt concentration (XPS), shows a significant concentration of Co^0-CO, while almost no CO seems to be adsorbed on the promoted catalysts. These results may indicate either that CO is readily dissociated at 220 °C, or that, probably due to a partial TiO_2 coverage, only few metallic Co is accessible on these catalysts [52]. This is typical of SMSI, which usually results in suppressed CO and H_2 chemisorption [102]. Therefore, partial coverage of metallic Co particles might be the reason for the low CO uptake and the different CO interaction strength observed during CO-TPD.

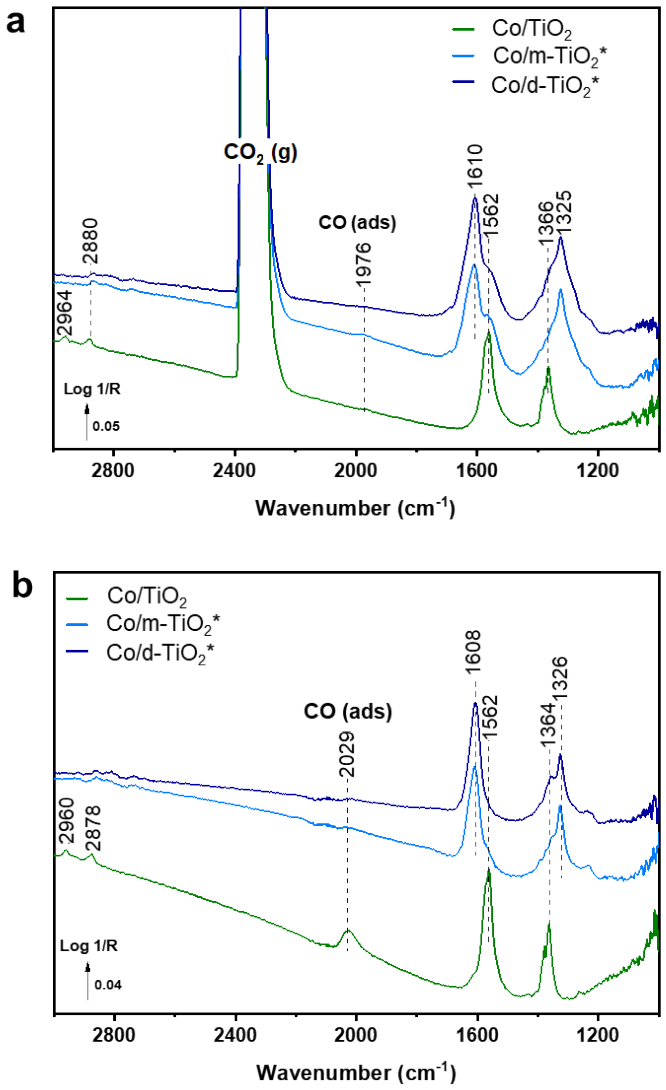

Figure 9. a) Operando DRIFT after 1 h of reaction with CO_2 at T = 220 °C, P = 1 bar (H_2/CO_2 = 2). **b)** Operando DRIFT after 1 h of reaction with CO at T = 220 °C, P = 1 bar (H_2/CO = 40).

The intensity of the cobalt carbonyl band was monitored down to 140 °C under the CO/H_2 stream (**Figure S31**), temperature at which conversion was negligible and surface coverage should have reached its maximum value [103]. These data show that the relative coverage at 220 °C was ca. 83% that at 140 °C over the unpromoted Co/TiO_2. The near absence Co-CO bands on the promoted sample cannot thus be mostly related to a temperature-dependent surface

coverage, but other effects are at play. We had previously mentioned that coverage of cobalt by TiO_x (SMSI effect) was a possible explanation for the lack of reduced cobalt at the sample surface. This was recently confirmed by a synchrotron-based near-ambient pressure X-ray photoelectron and absorption study performed under CO_2/H_2 at 250 °C [104]. We should add now that potential cobalt oxidation cannot be excluded under pressure. It had been shown over non-promoted Co/TiO_2 catalyst that CO_2 did not lead to cobalt oxidation [5], but this has not yet been proven on these B- and K-promoted samples, which could lead to more oxophilic cobalt particles.

At that point, the characterizations performed allow us to confirm a dual role of the promoter on catalyst activity. It allows CO_2 activation (medium/strongly adsorbed CO_2) when present on the support, which can explain the higher STY obtained on the Co/m-TiO_2* and Co/m-TiO_2*-reox catalysts compared to the unpromoted Co/TiO_2 catalyst. When there is a significant interaction between the promoter and the metal (Co/d-TiO_2* catalyst), a reduced H_2 activation induced a drop of the activity and a higher selectivity towards hydrocarbons, in agreement with what is known from the literature. Despite the fact that the promoter location (on the support or in contact with Co) is a key parameter for catalytic performance, a nice correlation was obtained between the total promoter content, independently of its location, and the X_{H2}/X_{CO2} ratio. The promoter can also favor the formation of surface defects, which in turn favor the development of SMSI effect, which is present in all the catalysts, but its degree is difficult to quantify. The O_v and Ti^{3+} defects on the catalysts, which could be present during CO_2-FTS at 20 bar, could also play a role on CO_2 activation. However, taken together, these results do not allow providing an explanation of the large difference in selectivity observed between the unpromoted catalyst (Co/TiO_2) and the two promoted catalysts, in which Na is mainly located on the support (Co/m-TiO_2* and Co/m-TiO_2*-reox). To explain this difference in selectivity, it is necessary to take into account that the CO_2 hydrogenation operates on a catalyst containing both the A-TiO_2 and R-TiO_2 phases on the same support.

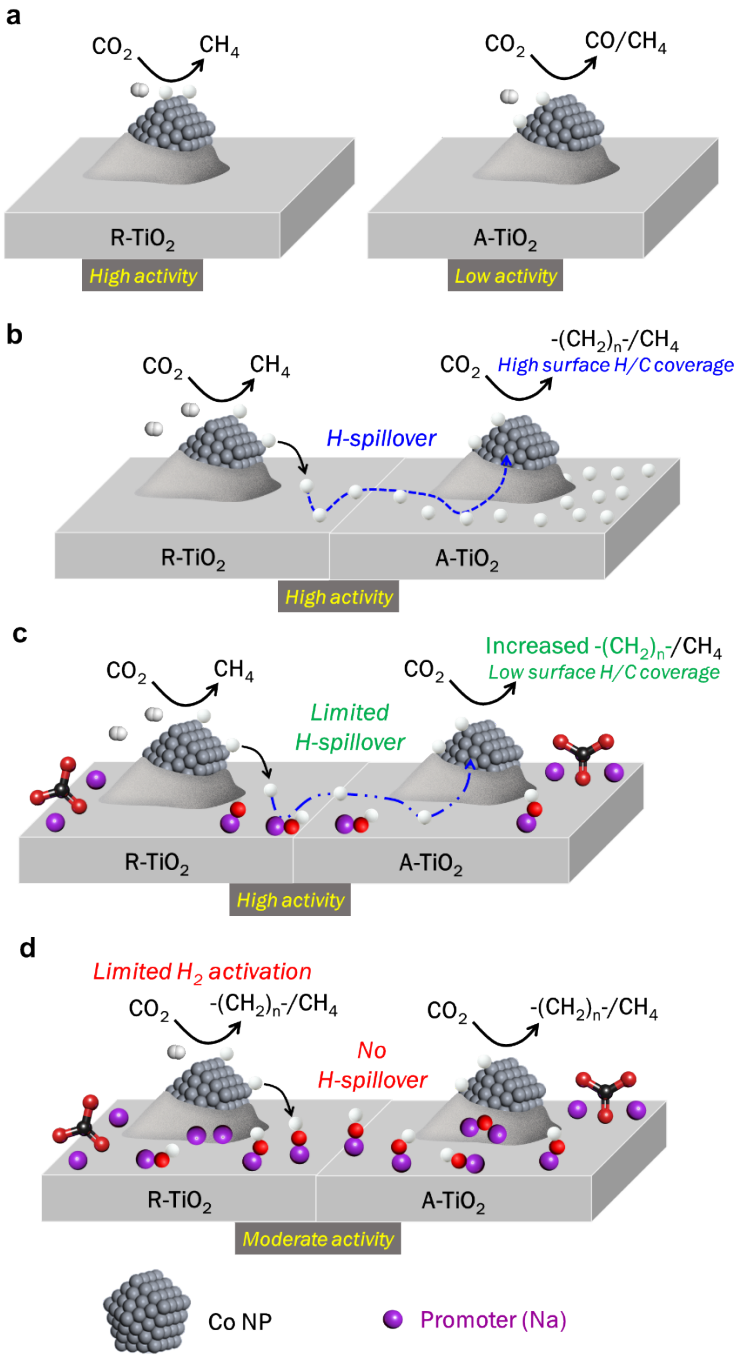

Figure 10. Mechanistic pathways for CO_2-based FTS at 220 °C on unpromoted and alkali-promoted Co/TiO_2 catalysts presenting SMSI. **a)**. Unpromoted Co/TiO_2 catalyst presenting different TiO_2 phases on different supports. **b)**. Unpromoted Co/TiO_2 catalyst presenting different TiO_2 phases on the same support (TiO_2-P25). **c)**. Alkali-promoted Co/TiO_2 catalyst presenting different TiO_2 phases on the same support (TiO_2-P25) and alkali on the support (Co/m-TiO_2* catalyst). **d)**. Alkali-promoted Co/TiO_2 catalyst presenting different TiO_2 phases on the same support (TiO_2-P25) and alkali on the support and on Co particles (Co/d-TiO_2* catalyst). Red spheres correspond to oxygen atoms and white spheres to hydrogen atoms.

It is known from the literature on CO_2 hydrogenation that Co/R-TiO_2 is very active and produces CH_4, while Co/A-TiO_2 is poorly active and more selective for CO production (**Figure 10a**) [16]. For conventional CO-FTS, the activity of Co/TiO_2 catalysts largely depends on the crystal phase of TiO_2 support [19, 105, 106]. At 230 °C and 10 bar, Shimura and coworkers

have shown that Co/R-TiO_2 is active for CO-FTS, and produces C_{5+} hydrocarbons with a good selectivity (68 %), while Co/A-TiO_2 is poorly active and also produces C_{5+} hydrocarbons with a good selectivity (72-75 %) [19]. Interestingly, the use of a mixture 15% R-TiO_2-85% A-TiO_2 as support allows increasing the activity compared to a 98%R-TiO_2 support, while maintaining a good selectivity towards C_{5+} hydrocarbons (66 %). However, the origin of the synergy between the two TiO_2 phases was not elucidated in that study. Furthermore, some of us have shown that for CO_2 methanation on Ni/TiO_2 catalysts, the catalytic activity depends appreciably on the nature of the support [107]. Adsorbed CO accumulates on the poorly active Ni/A-TiO_2 and not on the very active Ni/R-TiO_2. The use of Ni/TiO_2-P25 allows for a significant increase of the reaction rate related to Ni/R-TiO_2. In that case, the role of Ni/R-TiO_2 is to assist the hydrogenation of the CO adsorbed on Ni/A-TiO_2. The synergy operates thanks to H-spillover from Ni/R-TiO_2 to Ni/A-TiO_2. It is reasonable to propose that a similar synergy could operate on the unpromoted Co/TiO_2 catalyst (**Figure 10b**). H-spillover on Fe/TiO_2 [108], Ni/TiO_2 [109] and Co/TiO_2 [57, 110] catalysts has already been reported. Efficient H-spillover from Co/R-TiO_2 to Co/A-TiO_2 in the Co/TiO_2 catalyst should contribute to the poor C_{2+} selectivity of this catalyst, because of an excess of active *H species on Co/A-TiO_2 favoring CH_4 formation. It is also known that Na^+ species may act as a trap for dissociated hydrogen species, significantly reducing H-spillover and hydrogen mobility on the catalyst surface [111-114]. Consequently, we suspected that for the promoted catalysts, an additional role of the Na deposited on the support (present as sodium titanate) could be to regulate the H-spillover from Co/R-TiO_2 to Co/A-TiO_2 to maintain a lower surface H/C coverage on Co/A-TiO_2. This modulation of H-spillover (**Figure 10c**) allowed a higher selectivity compared to the unpromoted catalyst, while maintaining a good activity.

To confirm this hypothesis, we have evaluated the H-spillover on the Co/TiO_2, Co/m-TiO_2* and Co/d-TiO_2* catalysts. WO_3 was used to diagnose H_2 activation on these catalysts, since it is known that the spilt-over H species can migrate and readily react with WO_3 (yellow powder) to form dark blue H_xWO_3 [115]. It has to be noted that H_2 molecules can reduce the WO_3 only above 200 °C [116]. As expected, and shown in the photographs in **Figure 11** taken after treatment with H_2 at 180 °C for 30 min, the WO_3 alone exhibited an unchanged color after hydrogen treatment. In contrast, the Co/TiO_2 catalyst gave the darkest color of the tungsten species after H_2 treatment, demonstrating that hydrogen dissociation and spillover occurred.

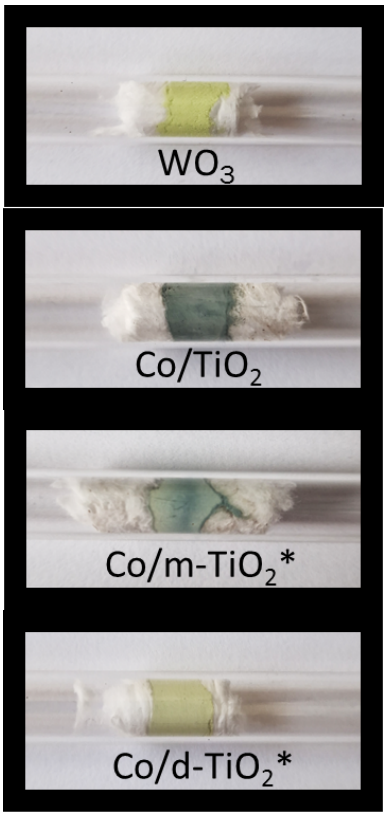

Figure 11. Photographs of samples made with 1 g of WO_3 mixed or not with 0.01 g of various catalysts after treatment with H_2 at 180 °C for 30 min.

The Co/m-TiO_2* catalyst also showed the color change, but the resultant color was lighter than that observed with the Co/TiO_2 catalyst, evidencing a reduced H-spillover for this catalyst presenting Na mainly on the support. Finally, for the Co/d-TiO_2* catalyst containing significant amounts of Na on the support and in interaction with Co particles, no H-spillover is observed. For this latter catalyst (**Figure 10d**), the presence of promoter in interaction with Co particles should lead to a drop in the exposed Co surface [89], to a lower H_2 activation [16, 41], and finally to a lower activity but good selectivity. Our catalytic tests also show that this phenomenon is more pronounced at 220 °C than at 250 °C, a temperature at which the Co/d-TiO_2* catalyst presented high activity and selectivity.

3. Conclusion

Supported Co-based catalysts synthesized on either unmodified or modified TiO_2 supports were developed and evaluated in CO_2 hydrogenation. The modification of the reducible oxide (TiO_2-P25, containing both rutile and anatase phases) consists in a thermal reduction with $NaBH_4$, which enable introducing surface defects (O_v and Ti^{3+}) and promoters (Na, B). The rutile TiO_2 phase is the most reactive one, resulting in the formation of a disordered TiO_2@TiO_{2-x} shell and a sodium titanate phase. The promoted cobalt catalysts contain various amounts of promoters as amorphous phases, which contribute to an increased CO_2 adsorption, but do not contain surface defects in appreciable concentration. All catalysts show similar electronic/geometric structure, a high level of cobalt reduction and present SMSI effect. The catalyst activity is not proportional to the amount of reduced Co, but to the amount of CO_2 they can medium/strongly adsorb. These results confirm that one role of the promoter is to assist CO_2 activation. The promoter concentration is nevertheless important, since a too high concentration results in a decrease in activity. This latter effect must be associated to a weaker activation of CO_2 that is

moderately/strongly bound, as seen from CO_2 TPD; but also, to the weaker activation of dihydrogen, because the excess of promoter interacts with the cobalt. Consequently, a second role of the promoter, if it interacts with cobalt, should be to limit H_2 activation, thus decreasing activity and increasing C_{5+} selectivity. Such a role of alkali promoters is well documented in CO-FTS and is also operative in CO_2-based FTS.

The promoted catalysts show significantly higher selectivity than the unpromoted one. To rationalize the effect of promoter on both activity and selectivity, it is necessary to take into account the existence of a cooperative catalysis between the Co on rutile TiO_2, which shows good activity but is selective for CH_4, and the Co on anatase TiO_2, which is poorly active and more selective to CO. The synergistic effect involves hydrogen spillover from the Co on rutile TiO_2 to the Co on anatase TiO_2. At moderate promoter loading, Na should be present mainly on the support, contributing to CO_2 activation. In parallel, the alkali promoter also slows down the H-spillover, contributing to maintaining a low surface H/C coverage of the Co on anatase TiO_2, resulting in significantly higher selectivity compared to the unpromoted catalyst. These results illustrate how surface promotion effects are valuable tools to adjust the FT product distribution toward the production of synthetic fuels.

4. Material and methods

4.1 Supports and catalysts preparation

m-TiO_2* support. 1 g of $NaBH_4$ (Aldrich, 99.99%) was dissolved in 50 mL of EtOH (Carlo Erba, 99.9 %) into a rotavapor flask. Then, the 10 g of TiO_2-P25 (Evonik, > 99.5 %) were added to the solution. The mixture was stirred in the rotavapor for 1 h (25 °C, 500 mbar). Subsequently, the EtOH was removed using the rotavapor (80 °C, 150 mbar for 30 min and then 75 mbar for 30 min). The resulting powder was dried overnight at 120 °C in a static oven, grinded and then treated in a tubular oven under argon at 320 °C, for 15 minutes (5 °C.min^{-1} ramp). Afterwards, the resulting blue product was recovered under Ar and then washed four times with distilled water, followed by washing with absolute ethanol. Finally, the product was dried for 15 h at 150 °C under argon (5 °C/min ramp).

d-TiO_2* support. 1.52 g of $NaBH_4$ was dissolved in 50 mL of EtOH into a rotavapor flask. Then, the 10 g of TiO_2-P25 were added to the solution. The mixture was stirred in the rotavapor for 1 h (25 °C, 500 mbar). Subsequently, the EtOH was removed using the rotavapor (80 °C, 150 mbar for 30 min and then 75 mbar for 30 min). The resulting powder was dried overnight at 120 °C in a static oven, grinded and then treated in a tubular oven under argon at 370 °C, for 30 minutes (5 °C.min^{-1} ramp). Afterwards, the resulting blue product was recovered under Ar and then washed four times with distilled water, followed by washing with absolute ethanol. Finally, the product was dried for 15 h at 150 °C under argon (5 °C/min ramp).

m-TiO_2*-reox support. The desired amount of m-TiO_2* support was placed in an alumina combustion boat and treated under air in a static oven at 350 °C for 30 minutes (5 °C/min ramp).

Cobalt catalysts. Cobalt catalysts with a loading of ~ 10 wt% were prepared via incipient wetness impregnation. For each catalyst, 10 g of the corresponding support were placed in a Schlenk vessel and degassed for 2 h under vacuum at 150 °C (oil bath temperature). After cooling down at room temperature, an aqueous metal precursor solution ($Co(NO_3)_2{\cdot}6H_2O$, Acros organic, 99 %) was added under vacuum and continuous stirring. The resulting mixture was sonicated for 30 min, followed by 30 min of stirring. The sonication/stirring sequence was repeated 4 times. The mixture was dried for 24 h at 80 °C followed by 12 h at 120 °C in a static furnace. Finally, the powder was treated in a tubular oven at 460 °C, for 4 h, under Ar (5 °C/min ramp).

***Catalyst reduction*.** For the characterizations of the reduced samples, 500 mg of catalyst were reduced in a tubular oven under a mixture of 40% H_2/Ar with a total flow of 25 mL·min^{-1}.

4.2 Supports and catalysts characterization

TEM and STEM measurements. Transmission electron microscopy (TEM) and scanning transmission electron microscopy (STEM) studies were performed using a JEOL cold-FEG JEM-ARM200F operated at 200kV equipped with a probe Cs corrector reaching a spatial resolution of 0.078 nm. EDX spectra were recorded with a JEOL CENTURIO SDD detector. The TEM analysis was performed on catalyst samples after the reduction steps. The catalyst samples were prepared by ultrasound-assisted dispersion in pure ethanol (Carlo Erba, 99.9 %), and the suspensions were dropped onto a holey carbon film-covered copper grid.

XRD measurements. XRD measurements were performed using a Panalytical Empyrean diffractometer equipped with a Co radiation source (l = 1.789 Å). The diffraction patterns of supports, calcined and reduced catalysts were recorded within the 2θ range of 20-95° with an increment of 0.02° and 400 s/step. The Scherrer equation was used for the determination of crystallite size. Anatase and rutile TiO_2 crystallite size were calculated from the peaks at 29.4° and 31.9°, respectively. Co_3O_4 crystallite size were calculated from the peak at 36.5°.

***Surface area measurements*.** The surface area was determined from N_2 adsorption/desorption isotherms at -196 °C using a Micromeritics 3Flex instrument. Prior to the analysis, all samples were degassed under vacuum at 200 °C for 5 h to remove physisorbed species.

***VSM*.** The magnetic measurements were performed using a Quantum Design Squid magnetometer at 300 K and field up to 6 T. The measurements were performed on reduced catalysts. Standard VSM capsules were filled with a known amount (a few mg) of sample and sealed. To avoid any oxidation, the samples were prepared in a glovebox, and transferred to the cryostat in a Schlenk vessel. The VSM capsule containing the sample was rapidly introduced into the VSM to avoid exposure of the sample to the air.

***H_2-temperature programmed reduction (TPR)*.** H_2-TPR measurements were performed using a Micromeritics AutoChem II 2920. In a typical experiment, 50 mg of catalyst were placed on quartz wool into a U-tube quartz reactor. The gases used were from Messer (quality 6.0). The sample was pretreated *in-situ* by ramping at 10 °C·min^{-1} to 350 °C under a He flow and remained at that temperature for 60 min. Subsequently, the sample was cooled down to 50 °C. At this temperature, a gas mixture of 5% H_2/N_2 passed through the sample with a total flow of 50 mL·min^{-1} and H_2-TPR was carried out by heating (10 °C min^{-1}) up to 900 °C. H_2 consumption was continuously monitored by a thermal conductivity detector.

***CO_2/CO-temperature programmed desorption (TPD)*.** The gases used were from Messer (quality 6.0). CO_2 (or CO) Temperature Programmed Desorption (TPD) measurements were carried out on a Micrometrics Auctochem II 2920 instrument equipped with a thermal conductivity detector. In a typical experiment, 150 mg of reduced catalyst were placed on quartz wool into a U-tube quartz reactor. The sample was pretreated *in-situ* by ramping at 10 °C.min^{-1} to 350 °C in a He flow and remained at that temperature for 60 min. Subsequently, the sample was cooled down to 50 °C. At this temperature, a gas mixture of 5% H_2/N_2 was sent on the sample with a total flow of 50 mL.min^{-1} and H_2-TPR was carried out by heating (10 °C.min^{-1}) up to 350 °C and held at this temperature for 30 min. H_2 consumption was continuously monitored by a thermal conductivity detector (TCD). Then, the gas flow was switched to He and held at 350 °C for 30 min. Subsequently, the sample was cooled down to 50 °C. At this

temperature, a gas mixture of 5% CO_2/N_2 (or 5% CO/He) was sent on the sample with a total flow of 50 mL.min^{-1} for 60 min. After saturation with CO_2 (or CO), the sample was outgassed for 60 min at 50 °C under He flow to ensure removal of physisorbed CO_2 (or CO). Finally, the sample was heated under He up to 900 °C with a ramp of 10 °C.min^{-1} to measure CO_2 (or CO) desorption (TCD). To assess sample basicity, the integral of the CO_2-TPD data was calculated for each data set and divided by the BET surface area of the respective sample.

EPR spectroscopy. Samples were placed in quartz EPR tubes (CFQ, OD 4 mm, Wilmad) and placed under helium atmosphere. EPR spectra were recorded on an X-band EMX-plus spectrometer (Bruker Biospin GmbH) equipped with a high-sensitivity resonator (ER4119HS, Bruker) and a variable temperature unit (ER4131VT, Bruker). Spectra were recorded at 100 K with a microwave power of 0.5 mW and a modulation amplitude of 0.4 mT.

XPS measurements. The quasi in situ laboratory-based XPS measurements were carried out in a custom-build ultrahigh-vacuum (UHV) setup coupled with a variable-pressure reactor (VPR) described in details elsewhere [117]. The four catalysts were initially reduced in a furnace at 350 °C for 4 hours under 1 bar 40% H_2/Ar flow and then stored for several weeks in air. About 100 mg of catalyst powder was pressed into a pellet and mounted on the XPS sample holder equipped with a boron nitride heater and a K-type thermocouple. Then the samples were subjected to a second reduction cycle, this time in the VPR reactor attached to the spectrometer under 7 mbar H_2 for 30 min at 400 °C. After the reduction treatment the VPR was evacuated and the sample was transferred under vacuum to the XPS chamber for analysis. All quasi in situ XPS spectra were collected under UHV ($1x10^{-8}$ mbar) at room temperature. A non-monochromatized Al Kα X-ray source was used, while survey and high-resolution spectra were recorded with analyzer pass energies of 90 and 22 eV respectively. Samples were exhibit mild charging upon measurements (up to 4 eV), therefore the presented binding energies were calibrated to the main C 1s peak at 284.6 eV. The reliability of this method was confirmed by the Ti 2p and O 1s peaks which after calibration gave practically identical binding energies for all catalysts.

XAFS measurements. Ex-situ X-Ray Absorption Fine Structure (XAFS) spectra were collected at BM23 beamline of European Synchrotron Radiation Facility (ESRF) [118] during beamtime allocated with the proposal CH-6666 [119]. Three ionization chambers were employed (I_0,I_1 and I_2) and filled with Ar:N_2 mixture. Co K-edge X-Ray Absorption Spectra (XAS) were collected in transmission mode on mass-optimized pellets of 13 mm^2 located between I_0 and I_1 while a Co metal foil was located before I_2. Step scan collection mode was employed in the 7570 – 8680 eV range with 0.3 eV/point energy resolution in the XANES region (7570 – 7700 eV) and 0.035 k/point resolution in the EXAFS region. 0.5 seconds/point integration time were employed leading to a total of 12 minutes/scan. Energy calibration and alignment, background subtraction and edge jump normalization were conducted with the Athena Software from Demeter Package [120]. Linear Combination Analysis (LCA) was done within the same software using CoO (Sigma Aldrich, >99.99%) and Co metal foil as reference spectra. Spectra were fit in the 7680 – 7820 eV range. The species concentration was constrained with values between 0 and 1 while their sum was not constrained to 1. FT-EXAFS spectra were extracted in the k range 3-13.8 Å^{-1} using Hanning window. All the reported FT-EXAFS fit were conducted with ARTEMIS software in the R range 1 – 3.6 Å [120]. Scattering amplitude factor (S_0^2) of 0.795 was evaluated from fit of metal foil (see Supporting Information for further details on the FT-EXAFS fit procedure).

Raman measurements. Raman characterization was done on a Horiba Labram HR Evolution spectrometer using a 532 nm laser excitation (ca. 5 mW) equipped with a Super Long Working Distance 50x objective and a 600 tr/mm grating (1.5 cm^{-1} resolution). Approximately 85 mg of sample was introduced in a Linkam CCR-1000 reaction cell. The Raman spectra were serially

acquired every 20 s after 20 s acquisition. Reduction of the solids took place from 20 °C to 340 °C (20 °C/min) in a H_2/N_2 flow at 20/30 mL.min^{-1} respectively followed by *ca*. 3.5 h at this temperature. Reaction was carried out by introducing at 220 °C, a reaction mixture containing $CO_2/H_2/N_2$ flow at 9/18/9 mL.min^{-1}, respectively. Band widths and positions were evaluated within the series by spectral treatment

DRIFTS measurements. *In situ* DRIFTS experiments were performed using a modified high temperature DRIFT cell from Spectra-Tech fitted with KBr windows placed in a Collector II assembly described elsewhere [121]. The spectrophotometer used was a Nicolet 8700 (ThermoFischer Scientific) fitted with a liquid-N_2 cooled MCT detector. The DRIFT spectra were recorded at a resolution of 4 cm^{-1} and 16 scans were averaged. The DRIFTS spectra are reported as log (1/R), where R is the sample reflectance. This pseudo-absorbance gives a better linear representation of the band intensity against surface coverage than that given by the Kubelka-Munk function for strongly absorbing media such as those based on metals supported on oxides [122]. The contribution of gas-phase CO was subtracted using a CO(g) spectrum collected under the same experimental conditions over powdered KBr. High purity gases He (99.999%), H_2 (99.999%), CO_2 (99.995%) and 5% CO/He (99.9%) from Air Liquide or Messer were used without further purification.

4.3 High-pressure catalytic tests

CO_2-FTS catalytic tests were performed in a high-pressure test rig illustrated in **Figure S32**. The gases used, N_2, H_2 and CO_2 (Messer) had a 99.9999% purity. The reactor is composed of a stainless-steel tube of 33 cm length and 14 mm inner diameter. For a given CO_2-FTS catalytic test, the bottom part of the reactor was filled with a Sasol Pural sintered α-Al_2O_3 (1000 °C, 5 h) to sustain the catalytic bed. Then, 2 g of calcined catalyst were diluted with 8 g of inert SiC (Alfa Aesar, > 98.5 %), and placed in the middle of the stainless-steel reactor tube. The rest of the tube was completed with calcined α-Al_2O_3. The separation between filling material (α-Al_2O_3) and catalyst was ensured by a layer of quartz wool. A thermocouple was placed at the center of the catalytic bed to control the reaction temperature. Each catalyst was reduced in-situ at 350 °C for 4 h under 40% H_2/N_2 with a total flow of 100 mL.min^{-1}. After reduction, the temperature was decreased to 220 °C and the catalyst was outgassed with N_2 to remove the excess of H_2. Then, the gas was switched to a mixture of $H_2/CO_2/N_2$ = 36/18/18 mL.min^{-1}. After 30 min, the pressure was slowly increased to 20 bar using a back-pressure controller. The test started once the desired pressure was reached. After the initial test at 220 °C, the temperature was increased to 250 °C.

The gaseous products were monitored every 30 min using an online μ-GC (Agilent 990) equipped with a MS5A SS (Ar carrier, Messer 6.0) column for the quantification of H_2, N_2, CH_4 and CO and a Poraplot U FS (He carrier, Messer 6.0) column for the quantification of CO_2, C_2H_4, C_2H_6, C_3H_8 and C_4H_{10}. Both columns are equipped with a TCD detector.

The condensable products were recovered using hot (150 °C) and cold (4 °C) condensers and analyzed by GC-Simdist (Shimazu GC-2010 Plus) equipped with ZB-1XT column and a flame ionization detector (FID). For the GC-SimDist analysis, the oil fractions of hot and cold condensers were mixed prior to performing the analysis. CS_2 was used as solvent.

The calculation on the gaseous products detected by m-GC were performed as follows.

N_2 was used as internal standard and the molar fraction of the different molecules during the CO_2-FTS were calculated as follow:

$$Z^{out}\,(\text{mL/min}) = \frac{\%Z}{\%N_2} \cdot N_2^{in}$$

Z^{out} = CO_2, H_2, CH_4, CO, C_2H_4, C_2H_6, C_3H_8, C_4H_{10}.

%Z is obtained directly from the μ-GC, which has an internal calibration. N_2^{in} = N_2 input flow.

CO_2 and H_2 conversions (X_{CO2}, X_{H2}) were calculated as follows:

$$X_{CO_2}(\%) = 100 \cdot \frac{CO_2^{in} - CO_2^{out}}{CO_2^{in}} \qquad X_{H_2}(\%) = 100 \cdot \frac{H_2^{in} - H_2^{out}}{H_2^{in}}$$

The selectivity of the different products (S_Z) were calculated as follows:

$$S_Z(\%) = 100 \cdot \frac{n \cdot Z^{out}}{CO_2^{in} - CO_2^{out}} \qquad S_{C_{5+}}(\%) = 100 - \Sigma S_Z$$

n = number of carbon atoms in Z.

The yields were calculated as follows:

$$Y_Z(\%) = \frac{X_{CO_2} \cdot S_Z}{100} \qquad Y_Z\left(mol_{CO_2 \text{converted to } Z} \cdot mol_{Me}^{-1} \cdot h^{-1}\right) = \frac{(Y_Z(\%)/100) \cdot CO_2^{in}\left(\frac{mol}{h}\right)}{mol_{Me}\,(mol)}$$

Z = CH_4, CO, C_{2+}, C_{5+}.

STY was calculated as follows:

$$STY\left(mol_{CO_2} \cdot mol_{Me}^{-1} \cdot h^{-1}\right) = \frac{(X_{CO_2}(\%)/100) \cdot CO_2^{in}\left(\frac{mol}{h}\right)}{mol_{Me}\,(mol)}$$

Author Contributions

C.S. carried out the synthesis, some structural characterizations, and catalytic tests. S.C. and G.V. performed the XRD characterizations and analyze the data. A.D. performed the spillover experiments. N.L.B. and A.K.B. performed the EPR characterizations and analyze the data. F.M. performed the DRIFTS characterizations and analyze the data. G.C. performed the Raman characterizations and analyze the data. M.B. and S.Z. performed the XPS characterizations and analyze the data. D. Salusso performed the XAS characterizations and analyze the data. K.S., D.P.M. and P.S. conceived and supervised the project. All authors discussed the results and commented on the manuscript. The manuscript was written through contributions of all authors. All authors have given approval to the final version of the manuscript.

Data availability

Data will be made available on request.

Declaration of competing interest

The authors declare that they have no known competing financial interests or personal relationships that could have appeared to influence the work reported in this paper.

Acknowledgements

This work was supported by the Agence Nationale de la Recherche (project ANR-19-CE07-0030), and was labeled by the EUR BIOECO under the "Investissements d'Avenir" program with reference ANR-18-EURE-0021, which are gratefully acknowledged. The authors thank Teresa Hungria (Centre de microcaractérisation Raimond Castaing) for the STEM-HAADF/EDX microscopy, and the technicians at the RAPSODEE center for technical CO_2-FTS tests.

References

[1] C. Panzone, R. Philippe, A. Chappaz, P. Fongarland, A. Bengaouer, Power-to-Liquid Catalytic CO_2 Valorization into Fuels and Chemicals: Focus on the Fischer-Tropsch Route. J. CO_2 Util. 38 (2020) 314-347.

[2] E. de Smit, B.M. Weckhuysen, The Renaissance of Iron-Based Fischer–Tropsch Synthesis: On the Multifaceted Catalyst Deactivation Behaviour. Chem. Soc. Rev. 37 (2008) 2758-2781.

[3] H. Schulz, Comparing Comparing Fischer-Tropsch Synthesis on Iron- and Cobalt Catalysts: The Dynamics of Structure and Function. In Stud. Surf. Sci. Catal., Davis, B. H.; Occelli, M. L., Eds. Elsevier: 2007, pp. 177-199.

[4] T. Lin, Y. An, F. Yu, K. Gong, H. Yu, C. Wang, Y. Sun, L. Zhong, Advances in Selectivity Control for Fischer–Tropsch Synthesis to Fuels and Chemicals with High Carbon Efficiency. ACS Catal. 12 (2022) 12092-12112.

[5] P. Bredy, D. Farrusseng, Y. Schuurman, F.C. Meunier, On the Link between Co Surface Coverage and Selectivity to CH_4 During CO_2 Hydrogenation over Supported Cobalt Catalysts. J. Catal. 411 (2022) 93-96.

[6] C. Scarfiello, D. Pham Minh, K. Soulantica, P. Serp, Oxide Supported Cobalt Catalysts for CO_2 Hydrogenation to Hydrocarbons: Recent Progress. Adv. Mater. Interf. 10 (2023) 2202516.

[7] I.C. ten Have, B.M. Weckhuysen, The Active Phase in Cobalt-Based Fischer-Tropsch Synthesis. Chem Catal. 1 (2021) 339-363.

[8] I.C.t. Have, J.J.G. Kromwijk, M. Monai, D. Ferri, E.B. Sterk, F. Meirer, B.M. Weckhuysen, Uncovering the Reaction Mechanism Behind Coo as Active Phase for CO_2 Hydrogenation. Nat. Commun. 13 (2022) 324.

[9] G. Melaet, W.T. Ralston, C.-S. Li, S. Alayoglu, K. An, N. Musselwhite, B. Kalkan, G.A. Somorjai, Evidence of Highly Active Cobalt Oxide Catalyst for the Fischer–Tropsch Synthesis and Co2 Hydrogenation. J. Am. Chem. Soc. 136 (2014) 2260-2263.

[10] S. Zhang, X. Liu, Z. Shao, H. Wang, Y. Sun, Direct CO_2 Hydrogenation to Ethanol over Supported Co_2C Catalysts: Studies on Support Effects and Mechanism. J. Catal. 382 (2020) 86-96.

[11] S. Zhang, X. Liu, H. Luo, Z. Wu, B. Wei, Z. Shao, C. Huang, K. Hua, L. Xia, J. Li, L. Liu, W. Ding, H. Wang, Y. Sun, Morphological Modulation of Co_2C by Surface-Adsorbed Species for Highly Effective Low-Temperature CO_2 Reduction. ACS Catal. 12 (2022) 8544-8557.

[12] T. Pu, W. Zhang, M. Zhu, Engineering Heterogeneous Catalysis with Strong Metal–Support Interactions: Characterization, Theory and Manipulation. Angew. Chem. Int. Ed. 62 (2023) e202212278.

[13] J. Jia, C. Qian, Y. Dong, Y.F. Li, H. Wang, M. Ghoussoub, K.T. Butler, A. Walsh, G.A. Ozin, Heterogeneous Catalytic Hydrogenation of CO_2 by Metal Oxides: Defect Engineering – Perfecting Imperfection. Chem. Soc. Rev. 46 (2017) 4631-4644.

[14] J. Lee, D.C. Sorescu, X. Deng, Electron-Induced Dissociation of CO_2 on TiO_2(110). J. Am. Chem. Soc. 133 (2011) 10066-10069.

[15] C. Qiu, Y. Odarchenko, Q. Meng, S. Xu, I. Lezcano-Gonzalez, P. Olalde-Velasco, F. Maccherozzi, L. Zanetti-Domingues, M. Martin-Fernandez, A.M. Beale, Resolving the Effect of Oxygen Vacancies on Co Nanostructures Using Soft Xas/X-Peem. ACS Catal. 12 (2022) 9125-9134.

[16] W. Li, G. Zhang, X. Jiang, Y. Liu, J. Zhu, F. Ding, Z. Liu, X. Guo, C. Song, CO_2 Hydrogenation on Unpromoted and M-Promoted Co/TiO_2 Catalysts (M = Zr, K, Cs): Effects of Crystal Phase of Supports and Metal–Support Interaction on Tuning Product Distribution, ACS Catal. 9 (2019) 2739-2751.

[17] N.A. Sholeha, H. Holilah, H. Bahruji, A. Ayub, N. Widiastuti, R. Ediati, A.A. Jalil, M. Ulfa, N. Masruchin, R.E. Nugraha, D. Prasetyoko, Recent Trend of Metal Promoter Role for CO_2 Hydrogenation to C_1 and C_{2+} Products. S. Afr. J. Chem. Eng. 44 (2023) 14-30.

[18] A.I. Tsiotsias, N.D. Charisiou, I.V. Yentekakis, M.A. Goula, The Role of Alkali and Alkaline Earth Metals in the CO_2 Methanation Reaction and the Combined Capture and Methanation of CO_2. Catalysts 10 (2020) 812.

[19] K. Shimura, T. Miyazawa, T. Hanaoka, S. Hirata, Fischer–Tropsch synthesis over TiO_2 supported cobalt catalyst: Effect of TiO_2 crystal phase and metal ion loading, Appl. Catal. A: Gen. 460-461 (2013) 8-14.

[20] M. Xing, W. Fang, M. Nasir, Y. Ma, J. Zhang, M. Anpo, Self-Doped Ti^{3+}-Enhanced TiO_2 Nanoparticles with a High-Performance Photocatalysis. J. Catal. 297 (2013) 236-243.

[21] H. Tan, Z. Zhao, M. Niu, C. Mao, D. Cao, D. Cheng, P. Feng, Z. Sun, A Facile and Versatile Method for Preparation of Colored TiO_2 with Enhanced Solar-Driven Photocatalytic Activity. Nanoscale 6 (2014) 10216-10223.

[22] S.A. Rawool, K.K. Yadav, V. Polshettiwar, Defective TiO_2 for Photocatalytic CO_2 Conversion to Fuels and Chemicals. Chem. Sci. 12 (2021) 4267-4299.

[23] M. Pradenas, J. Yáñez, S. Ranganathan, D. Contreras, P. Santander, H.D. Mansilla, Multivariate Approach to Hydrogenated TiO_2 Photocatalytic Activity under Visible Light. Water Environ. Res. 91 (2019) 157-164.

[24] X. Pan, M.-Q. Yang, X. Fu, N. Zhang, Y.-J. Xu, Defective TiO_2 with Oxygen Vacancies: Synthesis, Properties and Photocatalytic Applications. Nanoscale 5 (2013) 3601-3614.

[25] H. Tian, L. Hu, C. Zhang, S. Chen, J. Sheng, L. Mo, W. Liu, S. Dai, Enhanced Photovoltaic Performance of Dye-Sensitized Solar Cells Using a Highly Crystallized Mesoporous TiO_2 Electrode Modified by Boron Doping. J. Mater. Chem. 21 (2011) 863-868.

[26] S. Santangelo, G. Messina, G. Faggio, A. Donato, L. De Luca, N. Donato, A. Bonavita, G. Neri, Micro-Raman Analysis of Titanium Oxide/Carbon Nanotubes-Based Nanocomposites for Hydrogen Sensing Applications. J. Solid State Chem. 183 (2010) 2451-2455.

[27] J. Xu, J. Huang, S. Zhang, Z. Hong, F. Huang, Understanding the Surface Reduction of Nano Rutile and Anatase: Selective Breaking of Ti-O Bonds. Mater. Res. Bull. 121 (2020) 110617.

[28] X. Zhang, C. Wang, J. Chen, W. Zhu, A. Liao, Y. Li, J. Wang, L. Ma, Enhancement of the Field Emission from the TiO_2 Nanotube Arrays by Reducing in a $NaBH_4$ Solution. ACS Appl. Mater. Interf. 6 (2014) 20625-20633.

[29] H. Rahman, A. Norbert, P.S. Nair, J.A. Joseph, S. Shaji, U. Deshpande, J. Naduvath, S.A. S, R.R. Philip, Influence of Sodium Doping on the Material Properties and Photocatalytic Activity of Anatase Titanium Dioxide Nanotubes Prepared by Anodization. Opt. Mater. 134 (2022) 113172.

[30] T. Ohno, K. Sarukawa, K. Tokieda, M. Matsumura, Morphology of a TiO_2 Photocatalyst (Degussa, P-25) Consisting of Anatase and Rutile Crystalline Phases. J. Catal. 203 (2001) 82-86.

[31] Z. Tian, S. Du, X. Cheng, J. Zhang, F. Li, Z. Chen, Y. Lv, Y. Zhu, G. Liu, The Role of Oxygen Vacancy in Anatase to Rutile Transformation of TiO_2. Cryst. Growth Des. 22 (2022) 6852-6856.

[32] T. Su, Y. Yang, Y. Na, R. Fan, L. Li, L. Wei, B. Yang, W. Cao, An Insight into the Role of Oxygen Vacancy in Hydrogenated TiO_2 Nanocrystals in the Performance of Dye-Sensitized Solar Cells. ACS Appl. Mater. Interf. 7 (2015) 3754-3763.

[33] H. Li, K. Wang, W. Li, S. Cheng, K. Jiang, Molten Salt Electrochemical Synthesis of Sodium Titanates as High Performance Anode Materials for Sodium Ion Batteries. J. Mater. Chem. A 3 (2015) 16495-16500.

[34] M. He, J. Ji, B. Liu, H. Huang, Reduced TiO_2 with Tunable Oxygen Vacancies for Catalytic Oxidation of Formaldehyde at Room Temperature. Appl. Surf. Sci. 473 (2019) 934-942.

[35] W.R. Siah, H.O. Lintang, M. Shamsuddin, L. Yuliati, High Photocatalytic Activity of Mixed Anatase-Rutile Phases on Commercial TiO_2 Nanoparticles. IOP Conf. Ser.: Mater. Sci. Eng. 107 (2016) 012005.

[36] M.J. Uddin, F. Cesano, A.R. Chowdhury, T. Trad, S. Cravanzola, G. Martra, L. Mino, A. Zecchina, D. Scarano, Surface Structure and Phase Composition of TiO_2 P25 Particles after Thermal Treatments and Hf Etching. Front. Mater. 7 (2020) 192.

[37] S.A. Sabinas-Hernández, J.M. Gracia Jiménez, N.R. Silva González, M.P. Elizalde-González, U. Salazar-Kuri, S. Tehuacanero-Cuapa, Blue Titania: The Outcome of Defects, Crystalline-Disordered Core-Shell Structure, and Hydrophilicity Change. Nanomater. 12 (2022) 1501.

[38] S. Eaimsumang, P. Prataksanon, S. Pongstabodee, A. Luengnaruemitchai, Effect of Acid on the Crystalline Phase of TiO_2 Prepared by Hydrothermal Treatment and Its Application in the Oxidative Steam Reforming of Methanol. Res. Chem. Intermed. 46 (2020) 1235-1254.

[39] C. Zhang, Y. Li, Y. Wang, H. He, Sodium-Promoted Pd/Tio2 for Catalytic Oxidation of Formaldehyde at Ambient Temperature. Environ. Sci. Technol. 48 (2014) 5816-5822.

[40] X. Zhu, M. Shen, L.L. Lobban, R.G. Mallinson, Structural Effects of Na Promotion for High Water Gas Shift Activity on Pt–Na/TiO_2. J. Catal. 278 (2011) 123-132.

[41] Z. Shi, H. Yang, P. Gao, X. Li, L. Zhong, H. Wang, H. Liu, W. Wei, Y. Sun, Direct Conversion of Co2 to Long-Chain Hydrocarbon Fuels over K–Promoted CoCu/TiO_2 Catalysts. Catal. Today 311 (2018) 65-73.

[42] J. Kapica-Kozar, E. Kusiak-Nejman, A. Wanag, Ł. Kowalczyk, R.J. Wrobel, S. Mozia, A.W. Morawski, Alkali-Treated Titanium Dioxide as Adsorbent for CO_2 Capture from Air. Microporous Mesoporous Mater. 202 (2015) 241-249.

[43] K. Upendar, A. Sri Hari Kumar, N. Lingaiah, K.S. Rama Rao, P.S. Sai Prasad, Low-Temperature CO_2 Adsorption on Alkali Metal Titanate Nanotubes. Int. J. Greenh. Gas Control 10 (2012) 191-198.

[44] K.H. Cats, B.M. Weckhuysen, Combined Operando X-Ray Diffraction/Raman Spectroscopy of Catalytic Solids in the Laboratory: The Co/TiO_2 Fischer–Tropsch Synthesis Catalyst Showcase. ChemCatChem 8 (2016) 1531-1542.

[45] A.C. Ghogia, B.F. Machado, S. Cayez, A. Nzihou, P. Serp, K. Soulantica, D. Pham Minh, Beyond Confinement Effects in Fischer-Tropsch Co/CNT Catalysts. J. Catal. 397 (2021) 156-171.

[46] W. Fang, M. Xing, J. Zhang, New Approach to Prepare Ti^{3+} Self-Doped TiO_2 Via Nabh4 Reduction and Hydrochloric Acid Treatment. Appl. Catal. B: Environ. 160-161 (2014) 240-246.

[47] V.A. de la Peña O'Shea, M. Consuelo Álvarez Galván, A.E. Platero Prats, J.M. Campos-Martin, J.L.G. Fierro, Direct Evidence of the Smsi Decoration Effect: The Case of Co/TiO_2 Catalyst. Chem. Commun. 47 (2011) 7131-7133.

[48] J. Lee, S.P. Burt, C.A. Carrero, A.C. Alba-Rubio, I. Ro, B.J. O'Neill, H.J. Kim, D.H.K. Jackson, T.F. Kuech, I. Hermans, J.A. Dumesic, G.W. Huber, Stabilizing Cobalt Catalysts for Aqueous-Phase Reactions by Strong Metal-Support Interaction. J. Catal. 330 (2015) 19-27.

[49] C. Qiu, Y. Odarchenko, I. Lezcano-Gonzalez, Q. Meng, T. Slater, S. Xu, A.M. Beale, Visualising Co Nanoparticle Aggregation and Encapsulation in Co/TiO_2 catalysts and Its Mitigation through Surfactant Residues. J. Catal. 419 (2023) 58-67.

[50] Y. Zhang, W. Yan, H. Qi, X. Su, Y. Su, X. Liu, L. Li, X. Yang, Y. Huang, T. Zhang, Strong Metal–Support Interaction of Ru on TiO_2 Derived from the Co-Reduction Mechanism of $Ru_xTi_{1-x}O_2$ Interphase. ACS Catal. 12 (2022) 1697-1705.

[51] Y. Yamazaki, K. Mori, Y. Kuwahara, H. Kobayashi, H. Yamashita, Defect Engineering of Pt/TiO_{2-x} Photocatalysts Via Reduction Treatment Assisted by Hydrogen Spillover. ACS Appl. Mater. Interf. 13 (2021) 48669-48678.

[52] F. Bertella, P. Concepción, A. Martínez, TiO_2 Polymorph Dependent Smsi Effect in Co-Ru/TiO_2 Catalysts and Its Relevance to Fischer-Tropsch Synthesis. Catal. Today 289 (2017) 181-191.

[53] T.O. Eschemann, K.P. de Jong, Deactivation Behavior of Co/TiO_2 Catalysts During Fischer–Tropsch Synthesis. ACS Catal. 5 (2015) 3181-3188.

[54] P. Panagiotopoulou, D.I. Kondarides, Effects of Alkali Promotion of TiO_2 on the Chemisorptive Properties and Water–Gas Shift Activity of Supported Noble Metal Catalysts. J. Catal. 267 (2009) 57-66.

[55] Y. Zhu, D. Liu, M. Meng, H_2 Spillover Enhanced Hydrogenation Capability of TiO_2 Used for Photocatalytic Splitting of Water: A Traditional Phenomenon for New Applications. Chem. Commun. 50 (2014) 6049-6051.

[56] L.M. van Koppen, A. Iulian Dugulan, G. Leendert Bezemer, E.J.M. Hensen, Elucidating Deactivation of Titania-Supported Cobalt Fischer-Tropsch Catalysts under Simulated High Conversion Conditions. J. Catal. 420 (2023) 44-57.

[57] K. Yang, G. Zhou, Hydrogen Evolution/Spillover Effect of Single Cobalt Atom on Anatase Tio2 from First-Principles Calculations. Appl. Surf. Sci. 536 (2021) 147831.

[58] M. Quesada-Gonzalez, B.A.D. Williamson, C. Sotelo-Vazquez, A. Kafizas, N.D. Boscher, R. Quesada-Cabrera, D.O. Scanlon, C.J. Carmalt, I.P. Parkin, Deeper Understanding of Interstitial Boron-Doped Anatase Thin Films as a Multifunctional Layer through Theory and Experiment. J. Phys. Chem. C 122 (2018) 714-726.

[59] V. Papaefthimiou, T. Dintzer, M. Lebedeva, D. Teschner, M. Hävecker, A. Knop-Gericke, R. Schlögl, V. Pierron-Bohnes, E. Savinova, S. Zafeiratos, Probing Metal–Support Interaction in Reactive Environments: An in Situ Study of PtCo Bimetallic Nanoparticles Supported on TiO_2. J. Phys. Chem. C 116 (2012) 14342-14349.

[60] W. Luo, S. Zafeiratos, Tuning Morphology and Redox Properties of Cobalt Particles Supported on Oxides by an in between Graphene Layer. J. Phys. Chem. C 120 (2016) 14130-14139.

[61] S. Turczyniak, W. Luo, V. Papaefthimiou, N.S. Ramgir, M. Haevecker, A. Machocki, S. Zafeiratos, A Comparative Ambient Pressure X-Ray Photoelectron and Absorption Spectroscopy Study of Various Cobalt-Based Catalysts in Reactive Atmospheres. Top. Catal. 59 (2016) 532-542.

[62] T. Cai, X. Chen, J.K. Johnson, Y. Wu, J. Ma, D. Liu, C. Liang, Understanding and Improving the Kinetics of Bulk Carbonation on Sodium Carbonate. J. Phys. Chem. C 124 (2020) 23106-23115.

[63] R. Würz, M. Rusu, T. Schedel-Niedrig, M.C. Lux-Steiner, H. Bluhm, M. Hävecker, E. Kleimenov, A. Knop-Gericke, R. Schlögl, In Situ X-Ray Photoelectron Spectroscopy Study of the Oxidation of $CuGaSe_2$. Surf. Sci. 580 (2005) 80-94.

[64] M.D. Wadge, M.J. Carrington, H. Constantin, K. Orange, J. Greaves, M.T. Islam, K.M. Zakir Hossain, T.P. Cooper, Z.R. Kudrynskyi, R.M. Felfel, I. Ahmed, D.M. Grant, Characterization of Potential Nanoporous Sodium Titanate Film Formation on Ti_6Al_4V and TiO_2 Microspherical Substrates Via Wet-Chemical Alkaline Conversion. Mater. Charact. 185 (2022) 111760.

[65] R.A. Zárate, S. Fuentes, J.P. Wiff, V.M. Fuenzalida, A.L. Cabrera, Chemical Composition and Phase Identification of Sodium Titanate Nanostructures Grown from Titania by Hydrothermal Processing. J. Phys. Chem. Solids 68 (2007) 628-637.

[66] D. Kong, Y. Wang, S. Huang, Y.V. Lim, J. Zhang, L. Sun, B. Liu, T. Chen, P. Valdivia y Alvarado, H.Y. Yang, Surface Modification of $Na_2Ti_3O_7$ Nanofibre Arrays Using N-Doped Graphene Quantum Dots as Advanced Anodes for Sodium-Ion Batteries with Ultra-Stable and High-Rate Capability. J. Mater. Chem. A 7 (2019) 12751-12762.

[67] L. Wang, H. Yue, Z. Hua, H. Wang, X. Li, L. Li, Highly Active Pt/Na_xTiO_2 Catalyst for Low Temperature Formaldehyde Decomposition. Appl. Catal. B: Environ. 219 (2017) 301-313.

[68] M. Yang, J. Liu, S. Lee, B. Zugic, J. Huang, L.F. Allard, M. Flytzani-Stephanopoulos, A A Common Single-Site Pt(II)–$O(OH)_x$– Species Stabilized by Sodium on "Active" and "Inert" Supports Catalyzes the Water-Gas Shift Reaction. J. Am. Chem. Soc. 137 (2015) 3470-3473.

[69] L. Cano-Casanova, A. Ansón-Casaos, J. Hernández-Ferrer, A.M. Benito, W.K. Maser, N. Garro, M.A. Lillo-Ródenas, M.C. Román-Martínez, Surface-Enriched Boron-Doped TiO_2 Nanoparticles as Photocatalysts for Propene Oxidation. ACS Appl. Nano Mater. 5 (2022) 12527-12539.

[70] N. Lu, X. Quan, J. Li, S. Chen, H. Yu, G. Chen, Fabrication of Boron-Doped TiO_2 Nanotube Array Electrode and Investigation of Its Photoelectrochemical Capability. J. Phys. Chem. C 111 (2007) 11836-11842.

[71] W. Zhao, W. Ma, C. Chen, J. Zhao, Z. Shuai, Efficient Degradation of Toxic Organic Pollutants with $Ni_2O_3/TiO_{2-x}B_x$ under Visible Irradiation. J. Am. Chem. Soc. 126 (2004) 4782-4783.

[72] O.V. Netskina, D.I. Kochubey, I.P. Prosvirin, S.E. Malykhin, O.V. Komova, V.V. Kanazhevskiy, Y.G. Chukalkin, V.I. Bobrovskii, D.G. Kellerman, A.V. Ishchenko, V.I. Simagina, Cobalt-Boron Catalyst for $NaBH_4$ Hydrolysis: The State of the Active Component Forming from Cobalt Chloride in a Reaction Medium. Mol. Catal. 441 (2017) 100-108.

[73] N. Feng, F. Liu, M. Huang, A. Zheng, Q. Wang, T. Chen, G. Cao, J. Xu, J. Fan, F. Deng, Unravelling the Efficient Photocatalytic Activity of Boron-Induced Ti3+ Species in the Surface Layer of TiO_2. Sci. Reports 6 (2016) 34765.

[74] M.V. Dozzi, L. Artiglia, G. Granozzi, B. Ohtani, E. Selli, Photocatalytic Activity vs Structural Features of Titanium Dioxide Materials Singly Doped or Codoped with Fluorine and Boron. J. Phys. Chem. C 118 (2014) 25579-25589.

[75] J.H.A. Martens, H.F.J. Van 't Blik, R. Prins, Characterization of Supported Cobalt and Cobalt-Rhodium Catalysts: II. Temperature-Programmed Reduction (Tpr) and Oxidation (Tpo) of Co/TiO_2 and Co-Rh/TiO_2. J. Catal. 97 (1986) 200-209.

[76] G. Agostini, A. Piovano, L. Bertinetti, R. Pellegrini, G. Leofanti, E. Groppo, C. Lamberti, Effect of Different Face Centered Cubic Nanoparticle Distributions on Particle Size and Surface Area Determination: A Theoretical Study. J. Phys. Chem. C 118 (2014) 4085-4094.

[77] D. Salusso, E. Borfecchia, S. Bordiga, Combining X-Ray Diffraction and X-Ray Absorption Spectroscopy to Unveil Zn Local Environment in Zn-Doped ZrO^2 Catalysts. J. Phys. Chem. C 125 (2021) 22249-22261.

[78] Y. Yao, X. Liu, D. Hildebrandt, D. Glasser, The Effect of CO_2 on a Cobalt-Based Catalyst for Low Temperature Fischer–Tropsch Synthesis. Chem. Eng. J. 193-194 (2012) 318-327.

[79] K. Qin, Y. Men, S. Liu, J. Wang, Z. Li, D. Tian, T. Shi, W. An, X. Pan, L. Li, Direct Conversion of Carbon Dioxide to Liquid Hydrocarbons over K-Modified $CoFeO_x$/Zeolite Multifunctional Catalysts. J. CO_2 Util. 65 (2022) 102208.

[80] B. Liang, H. Duan, T. Sun, J. Ma, X. Liu, J. Xu, X. Su, Y. Huang, T. Zhang, Effect of Na Promoter on Fe-Based Catalyst for CO_2 Hydrogenation to Alkenes. ACS Sustain. Chem. Eng. 7 (2019) 925-932.

[81] I.K. van Ravenhorst, A.S. Hoffman, C. Vogt, A. Boubnov, N. Patra, R. Oord, C. Akatay, F. Meirer, S.R. Bare, B.M. Weckhuysen, On the Cobalt Carbide Formation in a Co/TiO_2 Fischer–Tropsch Synthesis Catalyst as Studied by High-Pressure, Long-Term Operando X-Ray Absorption and Diffraction. ACS Catal. 11 (2021) 2956-2967.

[82] R.-P. Ye, J. Ding, W. Gong, M.D. Argyle, Q. Zhong, Y. Wang, C.K. Russell, Z. Xu, A.G. Russell, Q. Li, M. Fan, Y.-G. Yao, CO_2 Hydrogenation to High-Value Products Via Heterogeneous Catalysis. Nat. Commun. 10 (2019) 5698.

[83] G. Prieto, Carbon Dioxide Hydrogenation into Higher Hydrocarbons and Oxygenates: Thermodynamic and Kinetic Bounds and Progress with Heterogeneous and Homogeneous Catalysis. ChemSusChem 10 (2017) 1056-1070.

[84] U. Rodemerck, M. Holeňa, E. Wagner, Q. Smejkal, A. Barkschat, M. Baerns, Catalyst Development for CO_2 Hydrogenation to Fuels. ChemCatChem 5 (2013) 1948-1955.

[85] J. Li, N.J. Coville, The Effect of Boron on the Catalyst Reducibility and Activity of Co/TiO_2 Fischer–Tropsch Catalysts. Appl. Catal. A: Gen. 181 (1999) 201-208.

[86] Z. Li, L. Zhong, F. Yu, Y. An, Y. Dai, Y. Yang, T. Lin, S. Li, H. Wang, P. Gao, Y. Sun, M. He, Effects of Sodium on the Catalytic Performance of Comn Catalysts for Fischer–Tropsch to Olefin Reactions. ACS Catal. 7 (2017) 3622-3631.

[87] P. Panagiotopoulou, D.I. Kondarides, Effects of Alkali Additives on the Physicochemical Characteristics and Chemisorptive Properties of Pt/TiO_2 Catalysts. J. Catal. 260 (2008) 141-149.

[88] J. Xie, P.P. Paalanen, T.W. van Deelen, B.M. Weckhuysen, M.J. Louwerse, K.P. de Jong, Promoted Cobalt Metal Catalysts Suitable for the Production of Lower Olefins from Natural Gas. Nat. Commun. 10 (2019) 167.

[89] K. Jeske, A.C. Kizilkaya, I. López-Luque, N. Pfänder, M. Bartsch, P. Concepción, G. Prieto, Design of Cobalt Fischer–Tropsch Catalysts for the Combined Production of Liquid Fuels and Olefin Chemicals from Hydrogen-Rich Syngas. ACS Catal. 11 (2021) 4784-4798.

[90] J.A. Delgado, C. Claver, S. Castillón, D. Curulla-Ferré, V.V. Ordomsky, C. Godard, Fischer–Tropsch Synthesis Catalysed by Small TiO_2 Supported Cobalt Nanoparticles Prepared by Sodium Borohydride Reduction. Appl. Catal. A: Gen. 513 (2016) 39-46.

[91] J. Li, N.J. Coville, Effect of Boron on the Sulfur Poisoning of Co/TiO_2 Fischer–Tropsch Catalysts. Appl. Catal. A: Gen. 208 (2001) 177-184.

[92] Z. Shi, H. Yang, P. Gao, X. Chen, H. Liu, L. Zhong, H. Wang, W. Wei, Y. Sun, Effect of Alkali Metals on the Performance of $CoCu/TiO_2$ Catalysts for CO_2 Hydrogenation to Long-Chain Hydrocarbons. Chin. J. Catal. 39 (2018) 1294-1302.

[93] B. Jongsomjit, T. Wongsalee, P. Praserthdam, Characteristics and Catalytic Properties of Co/TiO_2 for Various Rutile:Anatase Ratios. Catal. Commun. 6 (2005) 705-710.

[94] M.I. Baraton, G. Busca, M.C. Prieto, G. Ricchiardi, V.S. Escribano, On the Vibrational Spectra and Structure of $FeCrO_3$ and of the Ilmenite-Type Compounds $CoTiO_3$ and $NiTiO_3$. J. Solid State Chem. 112 (1994) 9-14.

[95] H. Mahir, Y. Brik, A. Benzaouak, E. La Greca, L. Consentino, M. Kacimi, A. El Hamidi, L.F. Liotta, Catalytic Performances of Co/TiO_2 Catalysts in the Oxidative Dehydrogenation of Ethane to Ethylene: Effect of $CoTiO_3$ and $CoTiO_4$ Phase Formation. Chemistry 5 (2023) 1518-1534.

[96] G. Busca, J. Lamotte, J.C. Lavalley, V. Lorenzelli, FT-IR Study of the Adsorption and Transformation of Formaldehyde on Oxide Surfaces. J. Am. Chem. Soc. 109 (1987) 5197-5202.

[97] J.M. Pigos, C.J. Brooks, G. Jacobs, B.H. Davis, Low Temperature Water–Gas Shift: The Effect of Alkali Doping on the Ch Bond of Formate over Pt/ZrO_2 Catalysts. Appl. Catal. A: Gen. 328 (2007) 14-26.

[98] K. Ito, H.J. Bernstein, The Vibrational Spectra of the Formate, Acetate, and Oxalate Ions. Can. J. Chem. 34 (1956) 170-178.

[99] L. Proaño, E. Tello, M.A. Arellano-Trevino, S. Wang, R.J. Farrauto, M. Cobo, In-Situ Drifts Study of Two-Step CO_2 Capture and Catalytic Methanation over Ru,"Na_2O"/Al_2O_3 Dual Functional Material. Appl. Surf. Sci. 479 (2019) 25-30.

[100] L.-P. Merkouri, J.L. Martín-Espejo, L.F. Bobadilla, J.A. Odriozola, A. Penkova, T. Ramirez Reina, M.S. Duyar, Unravelling the CO_2 Capture and Conversion Mechanism of a Niru–Na_2O Switchable Dual-Function Material in Various CO_2 Utilisation Reactions. J. Mater. Chem. A 11 (2023) 13209-13216.

[101] A.V. Grigorieva, V.V. Yuschenko, I.I. Ivanova, E.A. Goodilin, Y.D. Tretyakov, Chemical Tuning of Adsorption Properties of Titanate Nanotubes. J. Nanomater. 2012 (2012) 920483.

[102] C.-J. Pan, M.-C. Tsai, W.-N. Su, J. Rick, N.G. Akalework, A.K. Agegnehu, S.-Y. Cheng, B.-J. Hwang, Tuning/Exploiting Strong Metal-Support Interaction (Smsi) in Heterogeneous Catalysis. J. Taiwan Inst. Chem. Eng. 74 (2017) 154-186.

[103] J. Couble, D. Bianchi, Heats of adsorption of linearly adsorbed CO species on Co^{2+} and Co° sites of reduced Co/Al_2O_3 catalysts in relationship with the CO/H_2 reaction, Appl. Catal. A: Gen. 445-446 (2012) 1-13.

[104] D. Salusso, C. Scarfiello, A. Efimenko, D. Pham Minh, P. Serp, K. Soulantica, S. Zafeiratos, Direct Evidence of Dynamic Metal Support Interactions in Co/TiO_2 Catalysts by Near-Ambient Pressure X-ray Photoelectron Spectroscopy, Nanomater. 13 (2023) 2672.

[105] K. Shimura, T. Miyazawa, T. Hanaoka, S. Hirata, Factors influencing the activity of $Co/Ca/TiO_2$ catalyst for Fischer–Tropsch synthesis, Catal. Today 232 (2014) 2-10.

[106] C. Schulz, P. Kolb, D. Krupp, L. Ritter, A. Haas, M. Soorholtz, T. Emmerich Maldonado, T.B. Thiede, C. Knobloch, Preparation and High-Throughput Testing of TiO_2-Supported Co Catalysts for Fischer–Tropsch Synthesis. Catalysts 11 (2021) 352.

[107] D. Messou, V. Bernardin, F. Meunier, M.B. Ordoño, A. Urakawa, B.F. Machado, V. Collière, R. Philippe, P. Serp, C. Le Berre, Origin of the Synergistic Effect between TiO_2 Crystalline Phases in the Ni/TiO_2-Catalyzed CO_2 Methanation Reaction. J. Catal. 398 (2021) 14-28.

[108] C. Mao, J. Wang, Y. Zou, G. Qi, J.Y. Yang Loh, T. Zhang, M. Xia, J. Xu, F. Deng, M. Ghoussoub, N.P. Kherani, L. Wang, H. Shang, M. Li, J. Li, X. Liu, Z. Ai, G.A. Ozin, J. Zhao, L. Zhang, Hydrogen Spillover to Oxygen Vacancy of $TiO_{2-x}H_y$/Fe: Breaking the Scaling Relationship of Ammonia Synthesis. J. Am. Chem. Soc. 142 (2020) 17403-17412.

[109] Y. Yao, D.W. Goodman, Direct Evidence of Hydrogen Spillover from Ni to Cu on Ni–Cu Bimetallic Catalysts. J. Mol. Catal. A: Chem. 383-384 (2014) 239-242.

[110] S.-W. Ho, Surface Hydroxyls and Chemisorbed Hydrogen on Titania and Titania Supported Cobalt. J. Chin. Chem. Soc. 43 (1996) 155-163.

[111] T. Komaya, A.T. Bell, Z. Wengsieh, R. Gronsky, F. Engelke, T.S. King, M. Pruski, Effects of Sodium on the Structure and Fischer-Tropsch Synthesis Activity of Ru/TiO_2. J. Catal. 152 (1995) 350-359.

[112] D.O. Uner, M. Pruski, T.S. King, The Role of Alkali Promoters in Fischer-Tropsch Synthesis on Ru/SiO_2 Surfaces. Top. Catal. 2 (1995) 59-69.

[113] G.R. Gallaher, J.G. Goodwin, C.S. Huang, M. Houalla, XPS and Reaction Investigation of Alkali Promotion of Rh/La_2O_3. J. Catal. 140 (1993) 453-463.

[114] R.A. Ortega-Domínguez, J.A. Mendoza-Nieto, P. Hernández-Hipólito, F. Garrido-Sánchez, J. Escobar-Aguilar, S.A.I. Barri, D. Chadwick, T.E. Klimova, Influence of Na Content on Behavior of Nimo Catalysts Supported on Titania Nanotubes in Hydrodesulfurization. J. Catal. 329 (2015) 457-470.

[115] Y. Xi, Q. Zhang, H. Cheng, Mechanism of Hydrogen Spillover on Wo3(001) and Formation of H_xWO_3 (X = 0.125, 0.25, 0.375, and 0.5). J. Phys. Chem. C 118 (2014) 494-501.

[116] S. Khoobiar, Particle to Particle Migration of Hydrogen Atoms on Platinum—Alumina Catalysts from Particle to Neighboring Particles. J. Phys. Chem. 68 (1964) 411-412.

[117] L. Zhong, T. Kropp, W. Baaziz, O. Ersen, D. Teschner, R. Schlögl, M. Mavrikakis, S. Zafeiratos, Correlation Between Reactivity and Oxidation State of Cobalt Oxide Catalysts for CO Preferential Oxidation, ACS Catal. 9 (2019) 8325-8336.

[118] O. Mathon, A. Beteva, J. Borrel, D. Bugnazet, S. Gatla, R. Hino, I. Kantor, T. Mairs, M. Munoz, S. Pasternak, F. Perrin, S. Pascarelli, The Time-Resolved and Extreme Conditions Xas (Texas) Facility at the European Synchrotron Radiation Facility: The General-Purpose Exafs Bending-Magnet Beamline BM_{23}. J. Synchrotron Radiat. 22 (2015) 1548-1554.

[119] E. Azizov, Barreau, M., Borfecchia, E., Escolano-Casado, G., Salusso, D., Spuri, L., Zafeiratos, S., Investigation of CO_2 methanation over highly active Ni-doped CeO_2 catalysts: insights into the active nickel sites in: E.S.R. Facility (Ed.), 2026.

[120] B. Ravel, M. Newville, ATHENA, ARTEMIS, HEPHAESTUS: data analysis for X-ray absorption spectroscopy using IFEFFIT, J. Synchrotron Radiat. 12 (2005) 537-541.

[121] H. Li, M. Rivallan, F. Thibault-Starzyk, A. Travert, F.C. Meunier, Effective Bulk and Surface Temperatures of the Catalyst Bed of Ft-Ir Cells Used for in Situ and Operando Studies. PCCP 15 (2013) 7321-7327.

[122] J. Sirita, S. Phanichphant, F.C. Meunier, Quantitative Analysis of Adsorbate Concentrations by Diffuse Reflectance Ft-Ir. Anal. Chem. 79 (2007) 3912-3918.

Table of Contents graphic

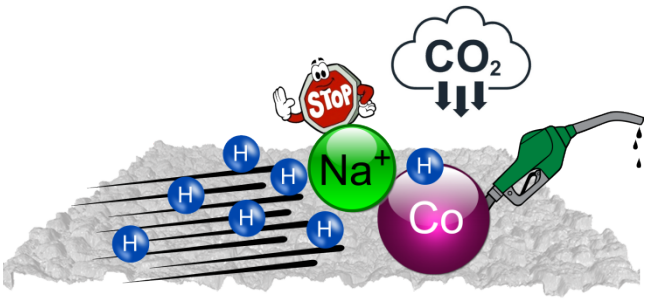

Highlights

Modified Co/TiO_2 catalysts for CO_2 hydrogenation to fuels

C. Scarfiello, K. Soulantica, S. Cayez, A. Durupt, G. Viau, N. Le Breton, A. K. Boudalis, F. Meunier, G. Clet, M. Barreau, D. Salusso, S. Zafeiratos, D. Pham Mihn, P. Serp

- Commercial TiO_2-P25 was partially reduced with $NaBH_4$, leading to the formation of oxygen vacancies, Ti^{3+} sites and the incorporation of Na.
- The catalyst activity is proportional to the amount of CO_2 they can medium/strongly adsorb.
- Catalysts prepared on modified supports outperform the one prepared on TiO_2-P25 in terms of activity and selectivity towards C_{5+}.
- The presence of alkali on the support contributes to the activation of CO_2 and allows a modulation of the hydrogen spillover in the system.
- A reduced H-spillover contributes to maintaining a low surface H/C coverage resulting in significantly higher selectivity compared to the unpromoted catalyst.

Declaration of interests

☒ The authors declare that they have no known competing financial interests or personal relationships that could have appeared to influence the work reported in this paper.

☐ The authors declare the following financial interests/personal relationships which may be considered as potential competing interests: